U.S. Department of Transportation

Federal Railroad Administration

Fatigue Crack Growth and Fracture Behavior of Bainitic Rail Steels

Office of Railroad
Policy and Development
Washington, DC 20590

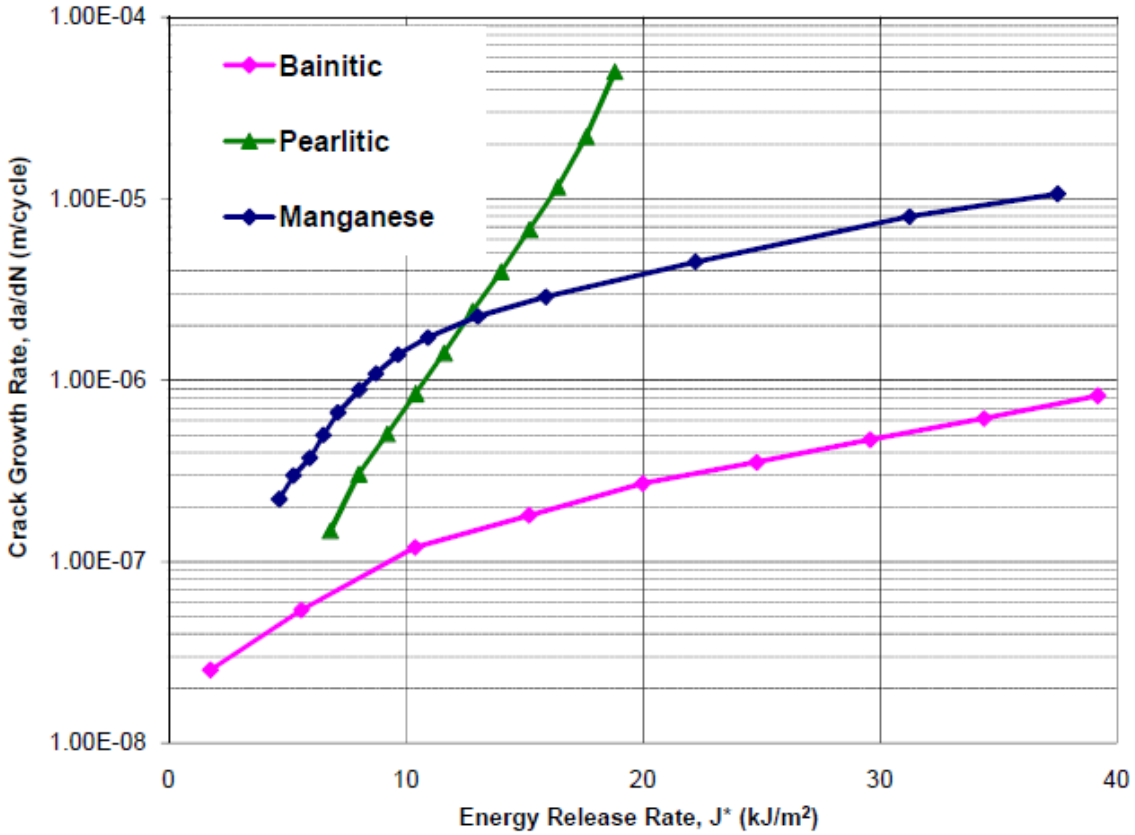

DOT/FRA/ORD-11/17

Final Report
September 2011

REPORT DOCUMENTATION PAGE

Form Approved
OMB No. 0704-0188

1. AGENCY USE ONLY (Leave blank)	2. REPORT DATE	3. REPORT TYPE AND DATES COVERED
	September 2011	Technical Report

4. TITLE AND SUBTITLE
Fatigue Crack Growth and Fracture Behavior of Bainitic Rail Steels

5. FUNDING NUMBERS
DTFR53-02-G-00021

6. AUTHOR(S)
Heshmat A. Aglan

7. PERFORMING ORGANIZATION NAME(S) AND ADDRESS(ES)
Tuskegee University
218 Foster Hall
Tuskegee, AL 36088

8. PERFORMING ORGANIZATION REPORT NUMBER

9. SPONSORING/MONITORING AGENCY NAME(S) AND ADDRESS(ES)
U.S. Department of Transportation
Federal Railroad Administration
Office of Railroad Policy and Development
Washington, DC 20590

10. SPONSORING/MONITORING AGENCY REPORT NUMBER
DOT/FRA/ORD-11/17

11. SUPPLEMENTARY NOTES
Program Manager: Mahmood Fateh

12a. DISTRIBUTION/AVAILABILITY STATEMENT
This document is available to the public through the FRA Web site at http://www.fra.dot.gov.

12b. DISTRIBUTION CODE

13. ABSTRACT (Maximum 200 words)
The microstructure–mechanical properties relationships, fracture toughness, fatigue crack growth and fracture surface morphology of J6 bainitic, manganese, and pearlitic rail steels were studied. Microstructure–mechanical properties correlation of the three rail steels under consideration revealed that the bainitic rail steel has the highest mechanical properties as compared with austenitic manganese steel (AMS) and pearlitic rail steels. AMS shows very few signs of being work hardened or toughened, which usually increases the mechanical properties of the material. In pearlite, the microstructure has more detailed features that contribute to its mechanical properties. The bainitic steel has more alloying elements that when mixed, create so many dislocations that the dislocations cannot move against each other. This is where bainitic steel derives its strength. Fracture toughness analysis (K_{Ic}) of the three rail steels, namely bainitic, manganese and pearlitic was performed. A valid K_{Ic} was determined for the pearlitic and bainitic steels based on the American Society of Testing and Materials (ASTM) E399 criteria. It was found that the pearlitic steel had an average K_{Ic} of 41 MPa $\sqrt{m}$ and the bainitic steel had an average value of 52 MPa $\sqrt{m}$. The manganese steel displayed elastic–plastic behavior, with a dominant plastic component. This invalidated the criteria of standard ASTM E399 and therefore a K_{Ic} could not be calculated. An approximate value for the energy release rate (680 kJ/m^2), based on ASTM standard E1820-01, was calculated instead for the manganese steel.

14. SUBJECT TERMS
bainitic, pearlitic, manganese rail steels, microstructure-mechanical property relationship, hardness, fracture toughness, fatigue crack growth

15. NUMBER OF PAGES
57

16. PRICE CODE

17. SECURITY CLASSIFICATION OF REPORT	18. SECURITY CLASSIFICATION OF THIS PAGE	19. SECURITY CLASSIFICATION OF ABSTRACT	20. LIMITATION OF ABSTRACT
Unclassified	Unclassified	Unclassified	

NSN 7540-01-280-5500

Standard Form 298 (Rev. 2-89)
Prescribed by ANSI Std. 239-18
298-102

Acknowledgments

The author wishes to acknowledge the financial support for this research project provided by the Federal Railroad Administration (FRA). The author wishes to thank Mr. Mahmood Fateh, FRA's Technical Representative, for his guidance during the course of this research, and Mr. Gunars Spons, FRA's Resident Engineer at the Transportation Technology Center (TTC) (Pueblo, CO) for his valuable support, including TTC field visits and the steel samples for the research. The author is also grateful to Dr. David Y. Jeong of the U.S. Department of Transportation Volpe Center (Cambridge, MA) for his input and insightful comments on the draft version of this report.

METRIC/ENGLISH CONVERSION FACTORS

ENGLISH TO METRIC	METRIC TO ENGLISH
LENGTH (APPROXIMATE)	**LENGTH (APPROXIMATE)**
1 inch (in) = 2.5 centimeters (cm)	1 millimeter (mm) = 0.04 inch (in)
1 foot (ft) = 30 centimeters (cm)	1 centimeter (cm) = 0.4 inch (in)
1 yard (yd) = 0.9 meter (m)	1 meter (m) = 3.3 feet (ft)
1 mile (mi) = 1.6 kilometers (km)	1 meter (m) = 1.1 yards (yd)
	1 kilometer (km) = 0.6 mile (mi)
AREA (APPROXIMATE)	**AREA (APPROXIMATE)**
1 square inch (sq in, in^2) = 6.5 square centimeters (cm^2)	1 square centimeter (cm^2) = 0.16 square inch (sq in, in^2)
1 square foot (sq ft, ft^2) = 0.09 square meter (m^2)	1 square meter (m^2) = 1.2 square yards (sq yd, yd^2)
1 square yard (sq yd, yd^2) = 0.8 square meter (m^2)	1 square kilometer (km^2) = 0.4 square mile (sq mi, mi^2)
1 square mile (sq mi, mi^2) = 2.6 square kilometers (km^2)	10,000 square meters (m^2) = 1 hectare (ha) = 2.5 acres
1 acre = 0.4 hectare (he) = 4,000 square meters (m^2)	
MASS - WEIGHT (APPROXIMATE)	**MASS - WEIGHT (APPROXIMATE)**
1 ounce (oz) = 28 grams (gm)	1 gram (gm) = 0.036 ounce (oz)
1 pound (lb) = 0.45 kilogram (kg)	1 kilogram (kg) = 2.2 pounds (lb)
1 short ton = 2,000 pounds (lb) = 0.9 tonne (t)	1 tonne (t) = 1,000 kilograms (kg)
	= 1.1 short tons
VOLUME (APPROXIMATE)	**VOLUME (APPROXIMATE)**
1 teaspoon (tsp) = 5 milliliters (ml)	1 milliliter (ml) = 0.03 fluid ounce (fl oz)
1 tablespoon (tbsp) = 15 milliliters (ml)	1 liter (l) = 2.1 pints (pt)
1 fluid ounce (fl oz) = 30 milliliters (ml)	1 liter (l) = 1.06 quarts (qt)
1 cup (c) = 0.24 liter (l)	1 liter (l) = 0.26 gallon (gal)
1 pint (pt) = 0.47 liter (l)	
1 quart (qt) = 0.96 liter (l)	
1 gallon (gal) = 3.8 liters (l)	
1 cubic foot (cu ft, ft^3) = 0.03 cubic meter (m^3)	1 cubic meter (m^3) = 36 cubic feet (cu ft, ft^3)
1 cubic yard (cu yd, yd^3) = 0.76 cubic meter (m^3)	1 cubic meter (m^3) = 1.3 cubic yards (cu yd, yd^3)
TEMPERATURE (EXACT)	**TEMPERATURE (EXACT)**
[(x-32)(5/9)] °F = y °C	[(9/5) y + 32] °C = x °F

QUICK INCH - CENTIMETER LENGTH CONVERSION

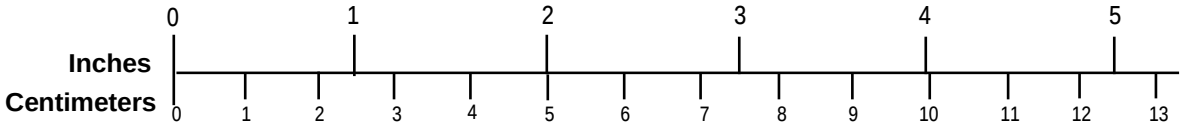

QUICK FAHRENHEIT - CELSIUS TEMPERATURE CONVERSIO

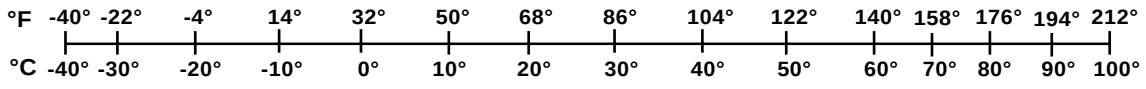

For more exact and or other conversion factors, see NIST Miscellaneous Publication 286, Units of Weights and Measures. Price $2.50 SD Catalog No. C13 10286

Updated 6/17/98

Contents

Illustrations

Tables

Executive Summary

The microstructure–mechanical properties relationships, fracture toughness, fatigue crack growth, and fracture surface morphology of J6 bainitic, manganese, and pearlitic rail steels were studied. Specimens were cut from the middle of each railhead along the longitudinal direction of the rail using electrical discharge machining. Fatigue crack propagation (FCP) tests were conducted under load control conditions using a servohydraulic Materials Testing System (MTS).

Microstructure–mechanical properties correlation of the three rail steels under consideration revealed that the bainitic rail steel has the highest mechanical properties as compared with austenitic manganese steel (AMS) and pearlitic rail steels. Examination of the microstructural features reveals that bainitic steel has a more intricate structure than AMS and pearlitic steels. AMS shows very few signs of being "work hardened" or toughened, which usually increases the mechanical properties of the material. Mostly large grains are present in the microstructure of AMS. In pearlite, the microstructure has more detailed features that contribute to its mechanical properties. The bainitic steel has more alloying elements that, when mixed, create so many dislocations that the dislocations cannot move against one another. This is where bainitic steel derives its strength.

Fracture toughness analysis (K_{Ic}) of the three rail steels, namely bainitic, manganese, and pearlitic, was performed. Compact tension specimens (½ T) were machined and fatigue precracked according to American Society of Testing and Materials (ASTM) standard E399. Multiple identical specimens from each material were tested using an 810 MTS with a 22-kilopound (kip) load cell. A valid K_{Ic} was determined for the pearlitic and bainitic steels, based on the ASTM E399 criteria. It was found that the pearlitic steel had an average K_{Ic} of 41 Megapascal-square root meter (MPa $\sqrt{m}$) and the bainitic steel had an average value of 52 MPa $\sqrt{m}$. The manganese steel displayed elastic–plastic behavior, with a dominant plastic component. This invalidated the criteria of standard ASTM E399, and therefore, a K_{Ic} could not be calculated. An approximate value for the energy release rate, based on ASTM standard E1820-01, was calculated instead for the manganese steel. An average value of 680 kJ/m^2 was obtained for the manganese steel.

Fatigue propagation tests, under load control, were performed on the three rail steels. Multiple identical specimens (at least three) were tested, and the average value of the FCP kinetics was taken. A simple form of the fatigue power law was used to rank the fatigue crack growth kinetics of the three materials. The results show that the bainitic steel has the highest fatigue damage tolerance as represented by the fatigue lifetime, FCP kinetics, and fatigue fracture surface morphological features. The fatigue damage tolerance of the manganese steel was superior to that of the pearlitic steel.

Fracture surface analysis of the fatigue failed specimens revealed the various mechanisms by which the bainitic steel acquired its superior resistance to fatigue crack growth. The bainitic rail steel displayed more ductile fracture features such as tearing and extensive disoriented ridge formation during the stable crack propagation process than the manganese and pearlitic steels. These features were responsible for the crack deceleration and indicate a considerably high-

energy consuming process associated with the crack propagation of the bainitic steel. Ductile flow-like tearing in the direction of crack propagation with feather-like pattern is observed on the fatigue fracture surface of the manganese steel in the stable crack propagation region. Pulled-up pearlitic lamella, limited microcracks, and microvoid coalescence were found on the fracture surface of the pearlitic rail steel during the stable crack process. The unstable crack propagation region of the bainitic steel exhibits both large and small dimples indicative of high resistance to material separation. The manganese steel, however, shows a limited number of dimples compared with the bainitic steel. Evidence of oriented tearing flow lines and ridges are apparent on its fracture surface at this high magnification. In contrast, cleavage and intergranular separation are associated with the unstable crack region of the pearlitic steel.

1. Introduction

Two types of steels are generally used for railroad applications: pearlitic and AMS. Bainitic steel has recently been considered as a candidate material for railroad applications. Pearlitic steel accounts for most of the steel tonnage that is produced today [1]. AMS alloy steel that exhibits a distinct combination of properties such as high toughness, resistance to wear, and heavy impact loading is commonly used in railway frogs [2]. Use of bainitic steel is now being explored because of the unique properties that it offers.

Pearlitic steel has a variety of alloying elements that include 0.72–0.8 percent carbon, 0.60–1.25 percent manganese, 0.10–0.60 percent silicon, 0.25–0.50 percent chromium, 0.25 percent nickel, with trace amounts of vanadium, molybdenum, sulfur, and phosphorus. Carbon is the main alloying element that has a variety of effects over a temperature range. Manganese is used in steel to reduce oxides and to improve the ductility and is often used in place of nickel to reduce the cost of the steel. Nickel and manganese both exhibit similar behavior when added to steel. Nickel increases the strength, ductility, and toughness of the steel. Silicon and vanadium reduce oxidation and serve as hardening agents. Tungsten promotes age hardening, refines the grain size, and increases the corrosion resistance and heat resistance of steel [3, 4]. Pearlitic steels gain their strength from the grains of pearlite within the microstructure. The alternating arrangement of lamellae that consists of cementite and ferrite increases the mechanical properties of the pearlitic steel. The microstructure consists of body-centered cubic (BCC) ferrite and BCC cementite. There are two main types of pearlitic steel: fine pearlite and course pearlite [5].

A typical AMS will contain 10–14 percent manganese, 0.95–1.4 percent carbon, and 0.3–1.00 percent silicon. Obtaining fully austenitic steels requires careful balancing of chemical composition. The most visible microstructural features of this single-phase alloy are the austenite grain boundaries. Austenite is also a rather soft, low-strength phase; however, work-hardening techniques produce substantial strengthening [6, 7]. The mechanical properties of AMS vary with both carbon and manganese contents. The grain size in austenitic manganese steel castings can vary widely and depends on the amount of superheat in the liquid metal during casting. The crystal structure of austenite is face-centered cubic (FCC) as compared with ferrite in bainitic and pearlitic, which has a BCC lattice. An FCC alloy has certain desirable characteristics; for example, it has low-temperature toughness and excellent weldability. Because of their FCC crystal structures, these alloys remain ductile irrespective of temperature or strain rate unless detrimental phase changes occur and are usually corrosion resistant [8].

Bainitic steel has a larger amount of alloying elements compared with pearlitic and AMS steels. Those elements are 0.23 percent carbon, 1.93 percent manganese, 1.96 percent silicon, 1.84 percent chromium, with less than 0.15 percent of nickel, copper, columbium, aluminum, vanadium, tungsten, boron, sulfur, and phosphorus. Because most bainitic steels have low carbon content, it increases the weldability of the steel. Also bainitic steel has a higher strength level and good ductility without the use of heat treatment. Boron increases the hardening of the steel; however, when used with molybdenum, it increases the tensile strength in both AMS and bainitic steel. Bainitic steels have large amounts of lath-shaped aggregates of ferrite and cementite within the microstructure. There are two main types of bainitic steel: upper and lower bainite. Upper bainite is formed in the temperature range of 400–550°C, contains parallel lath-

shape constituents of ferrite, and has a feathery appearance when viewed with optical microscopy. Lower bainite is formed in the region of 250–400°C and appears to have a more acicular morphology than upper bainite. Although the laths are similar and have the same width of 0.5 micrometers, laths of ferrite in lower bainite are much broader and more disoriented than upper bainite. It has been found that lower bainite has higher strength and toughness than upper bainite. The main assumption for this is the nucleation of the ferrite laths at the austenite grain boundaries as seen in upper bainite, but there is nucleation occurring within the grains themselves, producing additional dislocations. Bainitic steels get their strength from the dislocations found in the structure of the ferrite [9–12].

Bainitic rails appear to be a very promising new development in rail track technology that first appeared in the mid-1990s. Only a limited amount of research has so far been conducted on bainitic steels. Comparison between pearlitic, manganese, and bainitic rail steels [13–16] revealed superior flaking resistance, good wear resistance, and excellent weldability of bainitic rail steels. A detailed comparison of the wear characteristics of bainitic and pearlitic steel has been conducted, of which the results showed that the bainitic steels are potential candidates for wear-resistant rail application [17]. Su and Clayton [14] gave a review of experimental research on wheel-rail contact, pointing out that the use of bainitic rail steel remained a fertile area for research, and started their studies on rolling contact fatigue of pearlitic and bainitic steels. They found that rolling contact fatigue cracks are associated with plastic deformation and embryo cracks can be produced even under dry running conditions.

Studies on the failure behavior of rails have demonstrated that FCP and fracture is one of the major causes of derailment and other severe accidents [18]. The limitations of fracture toughness and fatigue strength criteria are obvious because of the diversified composition of rails and the complicated live and residual stress conditions. Efforts to study the fatigue behavior of rails have been made [18, 19]. For example, Orringer et al. [20–22] studied the FCP of detail fracture in rails. More recently, Glowacki and Kuziak [23] have investigated the effect of coupled thermal-mechanical processes on the evolution of microstructure in rails. Head-hardening behavior and rolling contact fatigue have also been studied [24, 25]. Fracture toughness and fatigue strength have been applied as criteria for characterization of the fatigue damage resistance of railway rails [26]. Another factor must be addressed that data on the fatigue properties of rails is considerably limited, which makes it difficult to further understand the fatigue behavior and to assess the fracture resistance of railway track alloys under cyclic loading conditions. Thus, it is necessary to acquire more fatigue data to study the related fracture and failure mechanisms and to propose new criterion of damage tolerance for rail steel materials. This is especially true for new materials, such as bainitic steel, if they are to be accepted in widespread application. So far, studies on the FCP behavior of bainitic rail steels have not been reported in the open literature.

To understand the relationships between the chemistry, manufacturing, and postprocessing and the mechanical properties of modern rails, a comprehensive review of such aspects is given. To obtain better track stability, longer rail life, reduced maintenance costs, reduced rail failure, and minimum interruptions to traffic, scrupulous materials selection, manufacturing procedures optimization and innovative track design have been proposed for a long time [27–32]. Among these various aspects, materials selection is the most basic one to achieve the above-mentioned goals. The following review will provide some information about the rail steel chemistry.

1.1 Chemistry of Rail Materials

Various metallurgical materials have been used for rail manufacturing. Cast metals and copper alloys are among those materials that have been used for a long time [33, 34]. However, copper alloys are not used as commonly as steel. Steel has been a universal material of choice for the manufacturing of rails ever since the beginning of the railway industry, primarily because of its cost-effectiveness. Although different manufacturing procedures such as quenching, hot rolling, etc., can change the mechanical properties of rails [35], the chemical composition of the steels remains the most essential factor that alters of the properties of rails [36, 37]. Medium carbon steel has been used for most of the sections of ordinary rails including upper table, lower table, web, foot, and head [38–41]. Most of the rails are rolled from open-hearth basic steel and contain from 0.50 to 0.60 percent by weight of carbon, from 0.90 to 1.20 percent manganese, from 0.10 to 0.30 percent silicon, and not more than 0.06 percent of sulfur and phosphorus [38]. Each element fulfills a different function in the steels. Iron is the basic element, whereas carbon serves as the most significant strengthening element. Silicon is a deoxidizing element. It increases the fluidity of the molten metal and condenses the alloy, thus producing solid ingots with fine grains. Phosphorus and sulfur harden the steel but decrease the ductility at much higher rates than any other element in the steels. Thus, the combination of the last two elements cause a brittle effect, and their presence is not desired in most cases.

Alloy steels are generally used for heavy-duty rails in places where high-stress concentration exists such as points, crossings, and sharp curves [42]. They are also used to make some special parts for rail stabilization, including, bearing-plates, fish-plates, spikes, fang-bolts, hook-bolts, Stewart's keys, chairs, open coiled keys, etc. Most of the commonly used alloy rail steels can be divided into three classes. These are medium manganese steel, high manganese steel, and chromium steel. Typically, medium manganese steel contains 1.10–1.40 weight percent (wt%) manganese and 0.45–0.55 wt% carbon. The content of silicon may be higher than 0.05 wt%, whereas the content of phosphorus and sulfur is generally lower than 0.05 wt%. High manganese steel contains higher manganese and higher carbon than the medium manganese steel. The composition of high manganese steel is manganese from 10.50 to 15.00 percent and carbon from 0.95 to 1.35 percent. Manganese hardens the steel, and provides more resistance to wear. However, manganese is expensive to use. In addition, the higher the content of manganese, the more difficult it is to manufacture the rails, because these factors imposed some limitations in the wide use of high manganese steel. Chromium steel has a typical composition of carbon from 0.42 to 0.53 percent, chromium from 0.75 to 1.00 percent, manganese from 0.65 to 0.85 percent. Chromium steels are even more expensive than manganese steels. Chromium steels are only used in rail joints or places where intensive traffic exists. The high cost of chromium steels may be partially offset with the reduction in maintenance and the increase in service lifetime.

1.2 Processing, Microstructure, and Heat Treatment of Premium Rail Steels

The microstructure of the premium rail steel is mainly pearlitic [43]. This provides the rail steel with excellent wear resistance. The premium steel can be made by open hearth, basic oxygen, or electric furnace, followed by a continuous casting process into hot topped ingots. To remove any undesired segregation, rolling has to be used in the manufacturing processes. The as-rolled rails will be fully heat treated or on-line hardened to achieve a head-hardening effect. Such procedures can further increase the wear resistance of the railhead made of the premium rail

steel. Following casting and hot rolling, one of the most important procedures in manufacturing premium rails is the head-hardening heat treatment. Such a treatment process can change the properties of the rail steel significantly. The head-hardening heat treatment is an on-line air-quenching process. It was found that it increases the hardness and yield strength of the rail steel significantly. It can also reduce strain softening in later use and thus can improve the deformation and wear resistance of the rail under service loading conditions. It was reported that heat treatment can increase the wear life of rails by at least 1,000 times [44, 45]. Beynon et al. [46] studied three pearlitic rail steels to investigate the head-hardening effect on the wear behavior of the steels. Comparative studies on several eutectoid steels were made. It was concluded that the head-hardened grade eutectoid steel had the highest resistance to rolling contact fatigue. The naturally hard eutectoid steel was the next best, whereas the lowest strength steel gave the worst wear performance. These researchers also studied the crack initiation behavior of these eutectoid steels. It was found that loading level is important in the formation of different shapes of cracks. Crack networks were formed in the specimens tested at nominal contact stresses of 1,200 and 1,500 MPa, whereas isolated cracks were produced in the specimens tested at 1,800 MPa.

1.3 Microstructure and Heat Treatment Influence on the Mechanical Properties of Premium Rail Steels

Although the contact fatigue resistance of rail steels can be increased significantly through head-hardening heat treatment such a heat treatment process can also exert adverse effects on tension/tension fatigue properties of the rail steels as reported by Hellier and Merati [47]. In their work, fatigue tests were conducted on single-edge–notched rectangular bar specimens machined from the head of a hardened heavy haul railway rail, manufactured using an ingot route. An increasing load technique was used for threshold determination with a small positive stress ratio R. The tests resulted in a fatigue threshold of 11.4 MPa $\sqrt{m}$ for $R = 0.11$, which is lower than the established fatigue threshold for standard carbon rail steel of approximately 14 MPa $\sqrt{m}$. In shear deformation dominated fatigue, the heat treatment caused an increase in the fatigue damage tolerance [48]. Rail rolling contact fatigue studies have been investigated, based on the performance of naturally hard and head-hardened rails in track by Muster et al. [25]. Rolling contact fatigue is reduced substantially by the use of harder rails. Fatigue defects occurred in the form of head splitting on the high rails of the curves; the phenomenon was much more pronounced for the non-heat-treated steel (naturally hard). Spalling defects also occurred in the case of the naturally hard steel. The naturally hard steel exceeds its ductility limit earlier because of pronounced cold deformation so that plastic shear deformations and ultimately cracking and spalling occur. On the contrary, the head-hardened rails prove far more resistant to contact fatigue damage because of their higher yield point. Cold deformation is much lower, so crack initiation becomes more difficult. In view of fatigue failure controlled by wear, the service life of head-hardened rails can therefore be expected to be much higher than that of the naturally hard rails.

Head-hardening heat treatment can also change the fracture toughness of the rail steels. Subsequently, the fracture and failure behavior of the rails can be altered. The relationship between fracture toughness and the failure behavior of rail steels is a very important aspect in the evaluation of the performance of rail steels. Singh et al. [49] presented the results on fracture toughness of standard carbon rail steel, wear-resistant rail steel, and two high-strength rail steels.

It has been found that, in contrast, higher wear resistance is usually achieved at a higher hardness of the rail steel; however, higher hardness can produce lower fracture toughness and higher fatigue crack growth rate. The quality of rails was evaluated by both the basic tensile properties and fracture toughness [50]. This was to establish the correlations between mechanical properties and fracture resistance as well as to calculate the critical flaw sizes inside rails.

During air quenching of the steels, phase transformation from austenite to pearlite occurs [51–54]. Because of the difference in cooling speed, the crystallization and grain growth kinetics of pearlite in different locations inside the railhead vary. The steel can be strengthened by solid solution, precipitation, increasing dislocation density, and pearlite volume fraction and grain-refining [55]. The microstructural change increases the hardness and tensile strength as often found in high carbon steel [56]. Microstructural effects, especially the grain size effect, have long been the focus in various metallic materials [57–59]. The microstructural effect on the tensile behavior of a ferrite-pearlite C-Mn steel has been studied by Hussain and De Los Rios [60]. This steel has a composition that is very similar to the rail steel. The ferrite phase in the direction of maximum shear stress has been identified as the preferable site for crack nucleation under tensile stress. Similar results have been reported by Nomura [61]. The ferrite precipitated along the austenite grain boundary is regarded as small cracks in medium carbon ferrite pearlite steels with fine prior austenite grain size. Thus, increase in carbon or alloy element contents such as manganese and vanadium contents raises the strength and fracture toughness through increasing the pearlite volume fraction and refining the ferrite grain size. Rosenberg and Kovove [62] investigated the influence of grain size on brittle fracture of medium carbon steel. The results indicated that resistance against brittle fracture evaluated by standard Charpy V-notch test in comparison with dynamic fracture toughness may give contradictory information about influence of microstructure.

1.4 Fatigue and Fracture Failure Behavior of Rail Steels

Various defects are normally the origins of fatigue failure. Efforts have been made to detect the formation of defects in rails by metallurgical and nondestructive methodologies [63–72]. Intensive studies on the wear and protection of rails have been performed in recent years [73, 74]. Wolfe, Spiegelberg, and Evangelisti [75] have used exploratory metallurgical evaluation of worn rails. Rail wear limits, based on rail strength investigations, have been estimated by Jeong, Tang, and Orringer [76]. Surface modification has been proposed to mitigate the wear and to prevent the formation of surface cracks on the rails [77, 78]. Laser modification [76] and diamond-like surface coating [77] have been applied to reduce the chance of failure.

Studies on the failure behavior of rails have demonstrated that FCP and fracture are two of the major reasons of derailment and other severe accidents [78]. Efforts to study the fatigue behavior of rails have been made [18, 78]. For example, Orringer [19–21, 67] studied the life of detail fracture in rails. More recently, Glowacki, and Kuziak [23] have investigated the effect of coupled thermal-mechanical processes on the evolution of microstructure in rails. Head-hardening behavior and rolling contact fatigue have been studied also [23, 79]. Fracture-toughness and fatigue-strength have been applied as criteria for characterization of the fatigue damage resistance of railway rails [25]. The limitations of fracture-toughness and fatigue-strength criteria are obvious because of the diversified composition of rails and the complicated life and residual stresses conditions. Another factor must be addressed in that data on the fatigue properties of rails is considerably limited, which makes it difficult to further

understand the fatigue behavior and to assess the fracture resistance of railway steel alloys under cyclic loading conditions. Thus, it is necessary to acquire more fatigue data, to study the related fracture and failure mechanism, and to propose new damage tolerance criteria for rail steels.

1.5 Scope

In this report, the microstructure–properties relationships, fatigue crack growth, and fracture surface morphology of bainitic rail steel, manganese rail steel, and conventional premium pearlitic rail steel are studied. Microdamage formation and evolution during crack movement, particularly on the fracture surface will be evaluated. The mechanical properties will be correlated with the microstructure of each material. The fatigue crack growth of the materials will be assessed and correlated with the fracture surface morphological features of the three rail steels. A simple form of the Paris equation will be used to rank the three materials.

2. Materials and Testing Methods

2.1 Materials Background

The materials used in the present study were a J6 bainitic rail steel and a pearlitic rail steel that was provided by the Transportation Technology Center, Inc. (Pueblo, CO), and a manganese rail steel that was provided by Nortrak of Birmingham, AL. No reported details on the manufacturing of the J6 bainitic rail are available, but it is believed that no heat treatment was done. The chemical compositions of the three steels are given in Table 1.

Table 1. Chemical Composition of the Bainitic, Manganese, and Pearlitic Rail Steel

Element	C	S	P	Si	Cr	Ni	Mn	Cu	Mo	Ti	Al	V	W	B
	% by weight													
Bainitic Steel	0.23	0.008	0.012	1.96	1.84	0.14	1.93	0.13	0.43	0.034	0.045	0.007	0.01	0.0047
Pearlite Steel	0.72–0.78	0.037	0.035	0.1–0.6	0.25–0.5	0.25	0.6–12.5	-	0.1	-	-	0.03–0.05	-	-
Manganese Steel	0.9–1.05	-	0.07	1 max	-	-	11.5–14	-	-	-	-	-	-	-

2.2 Specimen Preparation

Specimens were prepared from their specific railhead by using electrical discharge machining (EDM). For fatigue tests, the railhead was sliced into thin layers for the preparation of test specimens; the schematic representation can be seen in Figure 1. In the present study, the middle layer at a depth of approximately 20 millimeters (mm) from the top of the head was chosen for the fatigue tests.

The specimens have nominal dimensions of 152.3 mm in length, 100 mm in gauge length, 25.4 mm in width, and 2 mm in thickness. At the center of one free edge of the specimens, a 60° notch of 6.2 mm depth was introduced by using EDM. The notch depth to sample width ratio (a/W) was 0.24. The sample geometries for the unnotched and notched specimens are shown in Figure 2. For fracture toughness, ½ T were cut from railheads along the direction of the rail by using EDM. The geometry of the compact tension specimens is shown in Figure 3 along with its nominal dimensions.

Figure 1. Drawing of Railhead and Locations of Typical Slices for Tests

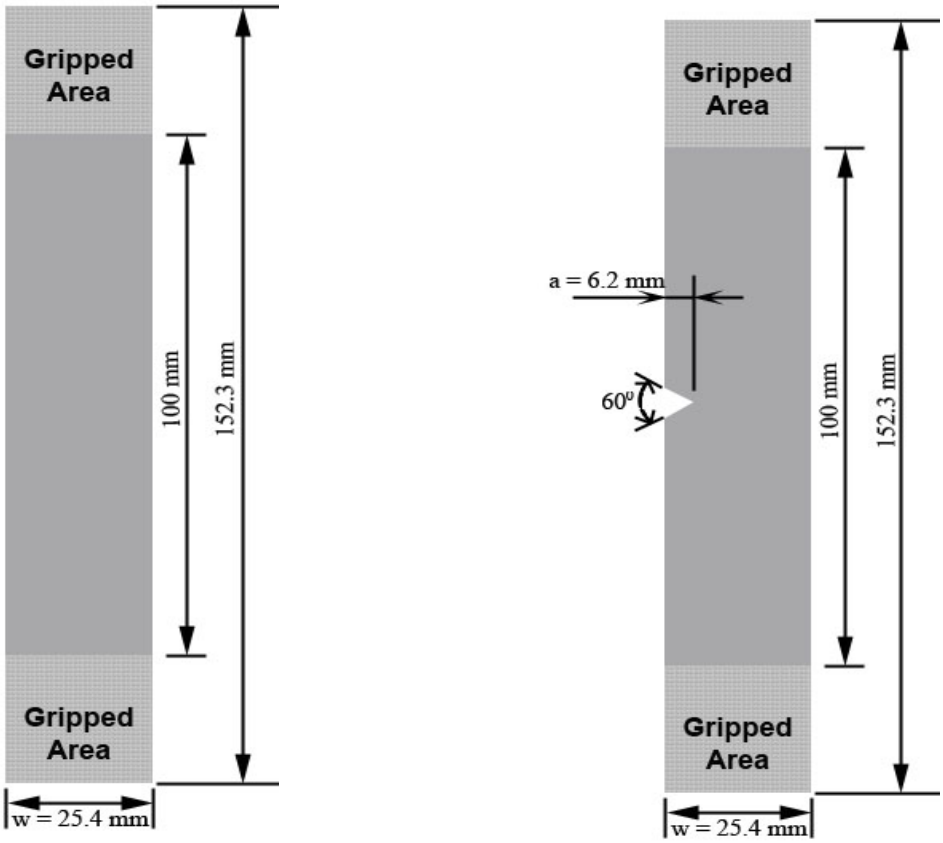

Tension Fatigue

Figure 2. Specimen Geometry

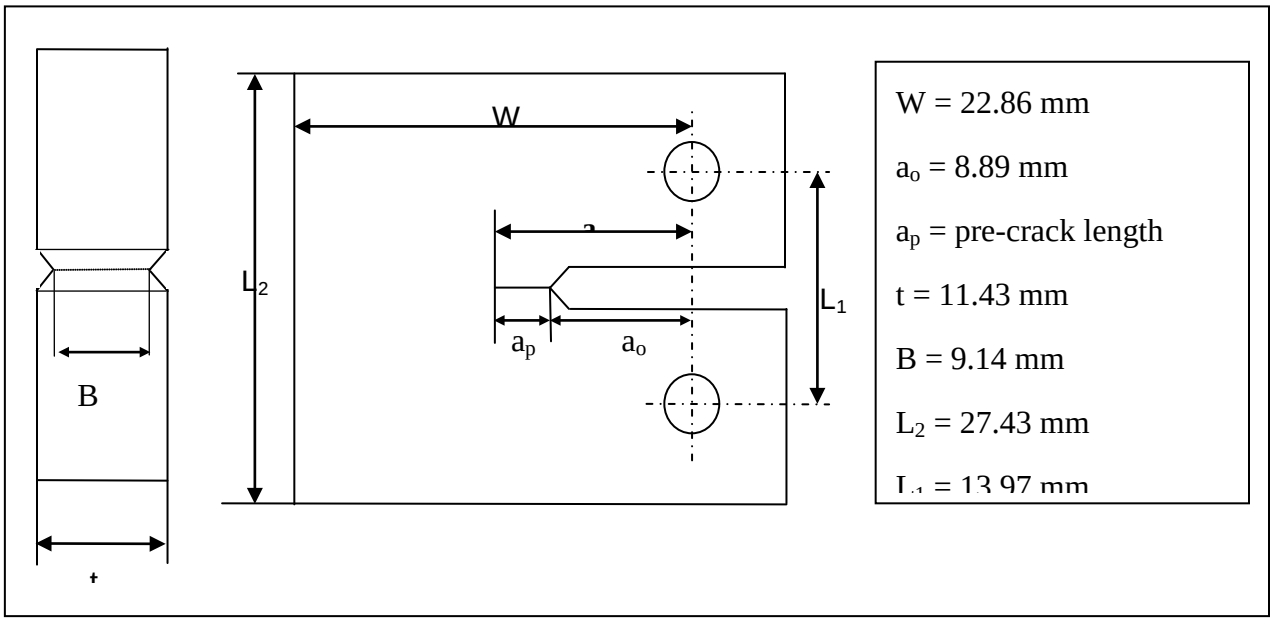

Figure 3. Compact Tension Specimens

2.3 Mechanical Testing

2.3.1 Static Tensile Tests

Static tensile experiments on unnotched specimens were performed using an 810 MTS equipped with a 100 kilonewton (kN) load cell. This was carried out under displacement control condition at a crosshead speed of 0.02 mm per second (s). The specimens were gripped between two hydraulic wedge grips typed 647.10A-01. The gage length was 100 mm. The static test results, based on the unnotched specimens, were used to calculate the ultimate strength of the rail steels.

2.3.2 Fracture Toughness

½ T were machined and fatigue precracked according ASTM standard E399. Multiple identical specimens (at least three) from each material were tested using an 810 MTS with a 22-kilopound load cell. The rate of loading was 20 kN per minute (min).

2.3.3 Fatigue Tests

FCP tests were conducted at room temperature of approximately 25°C under load control conditions using a sinusoidal waveform and a frequency of 1 hertz. The maximum stress was 200 MPa for the bainitic and pearlitic steels and 97 MPa for manganese steel, and the ratio of minimum stress to maximum stress was 0.1. The crack length at various intervals at a specific number of cycles was recorded during the tests. A video camera with a zoom lens was used to view the crack tip region, to measure the crack length, and to capture the damage associated with the crack growth. A total of three samples were tested from each material, and data from each sample was used for the FCP analysis and the fatigue damage species examination.

2.4 Microstructure and Fracture Surface Morphology Examination

The microstructures of the bainitic, manganese and the pearlitic rail steels were studied using an optical microscope. Various microstructural features of each rail steel were identified. The

fracture surfaces for all specimens were examined using a Hitachi S-2150 Scanning Electron Microscope operated at acceleration voltage of 20 kilovolts. Typical micrographs revealing the fracture surface morphology were taken using a PCI-Image Management System.

3. Microstructure and Mechanical Properties Relationships

3.1 Introduction

The materials used in the present work were bainitic, manganese, and pearlitic rail steels. The chemical composition of all three rail steels is given in Table 1. Small samples were sectioned from the regular rectangular specimens and mounted on an epoxy mold of 1.25 inches in diameter. The samples were polished using both a BETA/VECTOR and the MINIMET 1000 Polisher/Grinder according to ASTM A128. The samples were then etched in 2-percent Nital solution for 60 s. The optical microstructures were taken with an OLYMPUS GX51 Inverted System Metallurgical Microscope with a Pixelink C-Mount digital camera and PAX-IT version 5.4a Windows-based imaging system. Rectangular specimens with a length of 150 mm, a width of 25.4 mm, and a thickness of 2 mm were sectioned from the middle of each rail were used for the mechanical properties evaluation.

Air quenching is normally done on the top layer of pearlitic steel rails [22]. Static tensile tests of the specimens were performed using a MTS 810 servohydraulic machine equipped with a 100-kilonewton load cell and controlled by the MTS TestStar II hardware and software. Displacement control conditions with a crosshead speed of 0.02 mm/s were used to carry out the static tests. The gage length for the specimens was 100 mm. Force and displacement data was acquired in real-time mode using the PC.

3.2 Results and Discussion

The stress–strain relationships of the three rail steels are shown in Figure 4, and a summary of their mechanical properties is given in Table 2. Bainitic steel has the highest yield strength, ultimate strength, and strain to failure as compared with both the pearlitic and AMS steels. Optical global microstructural features, at 100×, for the three materials are shown in Figure 5. The microstructure of the bainitic steel is seen to be very intricate. The high mechanical properties found in the bainitic steel correspond to the low amount of carbon and the increased amount of other alloying elements in the chemical composition. An increase in the amount of alloying elements in the pearlitic rail steel as compared with the manganese steel has made a contribution to the increased mechanical properties, compared with the AMS steel. Other processing methods such as heat treatment can play a part in the strength of the pearlitic steel. The microstructure of the AMS is an indication of a soft material, with no work hardening having taken place. If manganese has not been work hardened, the material will have low mechanical properties. Also, AMS has a relatively low amount of alloying elements in its chemical composition. The manganese steel has only four to six alloying elements. The mechanical properties of AMS is in the same range as those found in the as cast properties.

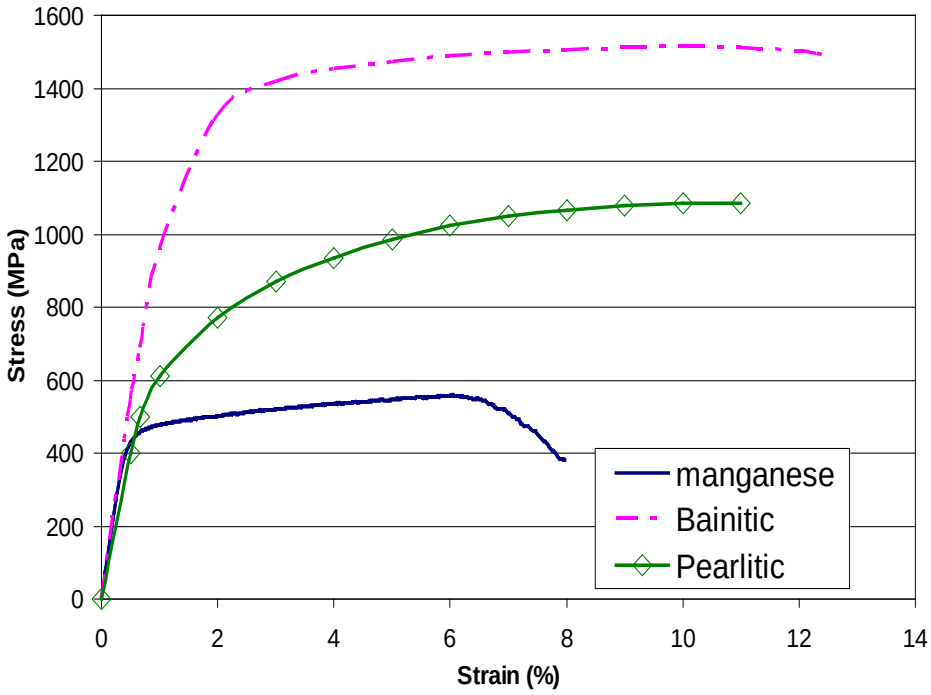

Figure 4. Stress–Strain Diagram of Manganese, Bainitic, and Pearlitic Steel

Table 2. Mechanical Properties of Pearlitic, AMS, and Bainitic Steel

Material	Yield Strength (Offset=0.2%) (MPa)	Ultimate Strength (MPa)	Failure Strain (%)
Pearlitic	700	1100	11
AMS	400	575	8
Bainitic	1100	1550	12.5

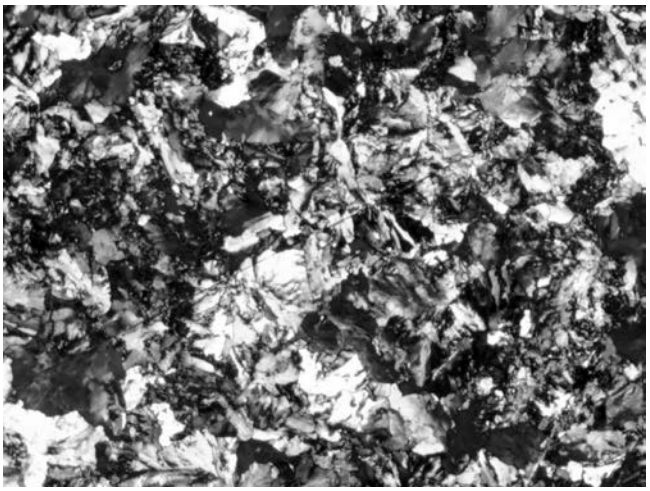

(a) Pearlitic Rail Steel

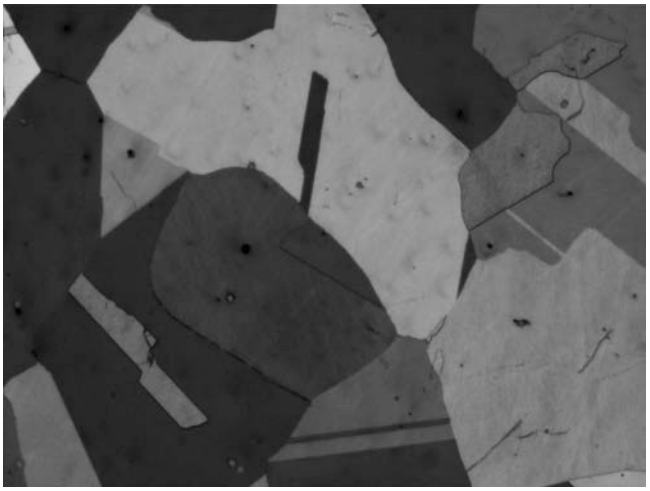

(b) Manganese Rail Steel

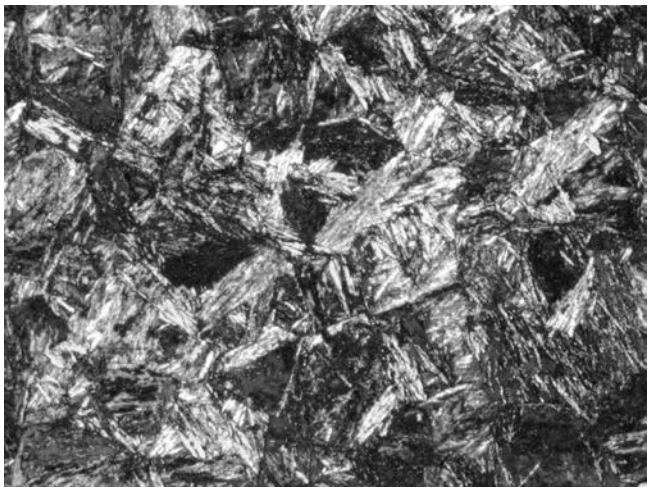

(c) Bainitic Rail Steel

Figure 5. Optical Global Microstructural Features, at 100× of (a) Pearlitic Rail Steel, (b) Manganese Rail Steel, and (c) Bainitic Rail steel

3.2.1 Microstructure of Pearlitic Rail Steel

The microstructure of pearlitic rail steel at 1,000× is shown in Figure 6. This steel has a lower amount of alloying elements than bainite but more alloying elements than the manganese. Each pearlitic grain has its own orientation. The lamellae of ferrite and cementite, with pearlite spectral, are seen throughout the grains. The lamellae are orientated in the same direction within each grain. At this higher magnification, the spacing of lamellae is clear. The mechanical properties of the pearlitic steel are determined by the interlayer spacing of the lamellae of the ferrite and cementite. The formation of ferrite and cementite is clearly shown at grain boundaries, with some parent austenite remaining in the grains.

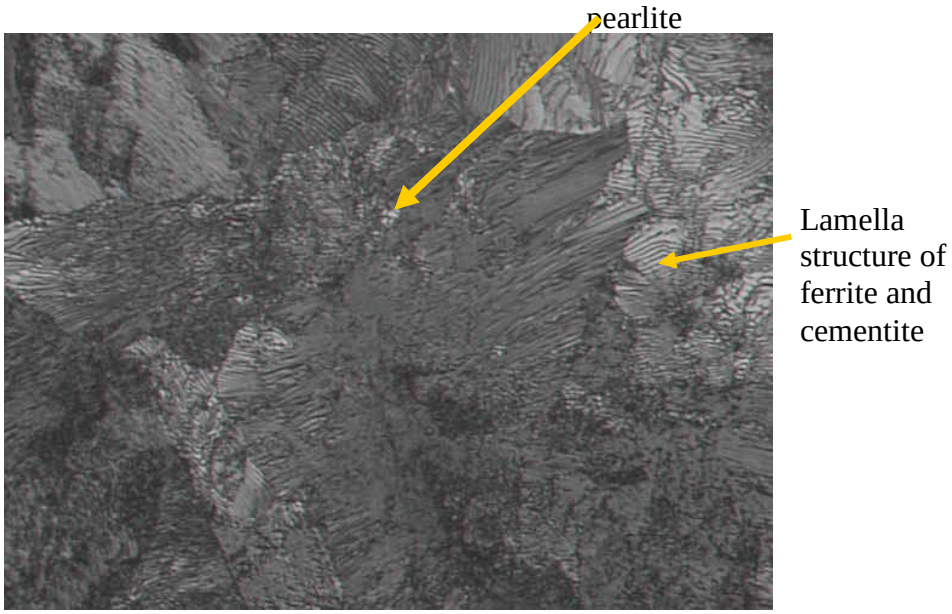

Figure 6. Optical Microstructure of the Pearlitic Rail Steel at 1,000×

3.2.2 Microstructure of Manganese Rail Steel

Typical microstructural features of AMS are shown in Figure 7 at 1,000× magnification. The grain boundaries seen in the AMS are very clear and well defined. Austenite is formed at higher temperatures than pearlite and bainite; therefore, more dislocations are present in AMS. Pitting and other inclusions can form dislocation loops in the microstructure. Pitting, which is often seen in the microstructure of AMS, is seen in Figure 7 on the left side. The dislocation loops formed can cause a decrease in the mechanical properties. Twinning, a phenomenon that also provides strength in AMS, is seen in the larger grain of this micrograph. This is an as-cast manganese sample that has not been heat treated or work hardened. The microstructure is representative of a single-phase alloy of an austenite matrix with cementite and a few patches of pearlite present. The patches of pearlite often provide additional strength for the material. Inhomogeneity of the grains that exists in the microstructure has resulted in the segregation of the alloying elements and carbide precipitation. Since manganese is a carbide-forming element, a sufficient amount is present to reduce the mechanical properties in the material.

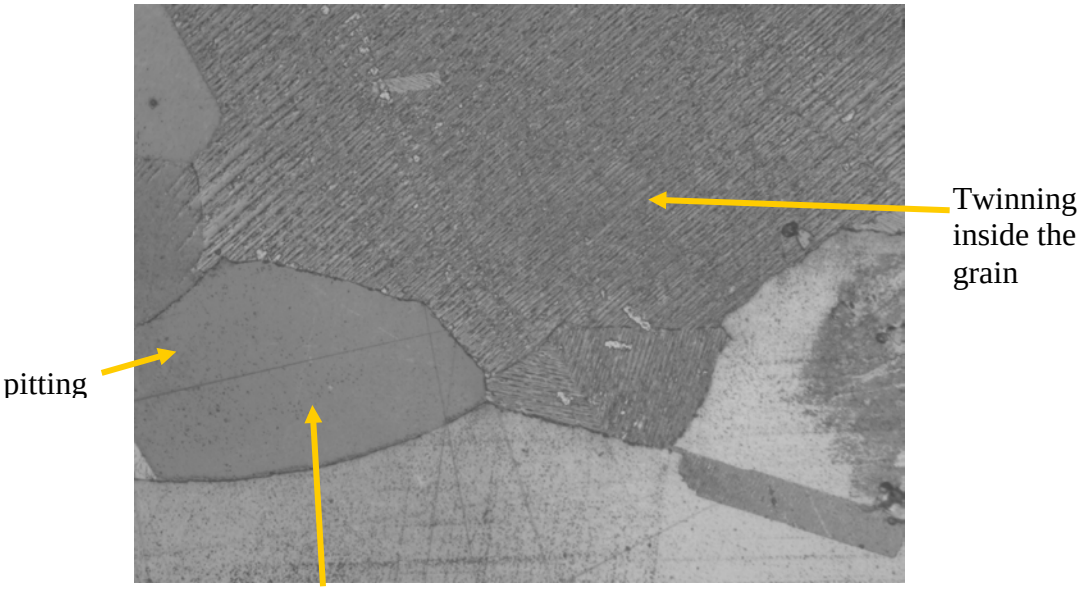

Figure 7. Optical Microstructure of the AMS Rail Steel at 1,000×

3.2.3 Microstructure of Bainitic Rail Steel

The microstructure of bainitic rail steel at 1,000× is shown in Figure 8. The grain boundaries are thin and clear in the bainitic sample. Primary laths formed at the grain boundary and secondary laths were formed from the primary laths within the grains. The cementite, which also forms parallel groups, did not fully precipitate in the ferrite laths. The laths are of parallel orientation within the grains, depending on the formation of the ferrite. This microstructure resembles a mixture of upper and lower bainite. In Figure 8, the bright parts with some dark spectral within are ferrite and upper bainite. The dark portion as indicated by the arrows is lower bainite. The intricate structure within the bainitic steel is caused by the low amount of carbon, the large amount of alloying elements, and the wide range of cooling rates used to process the bainitic steel.

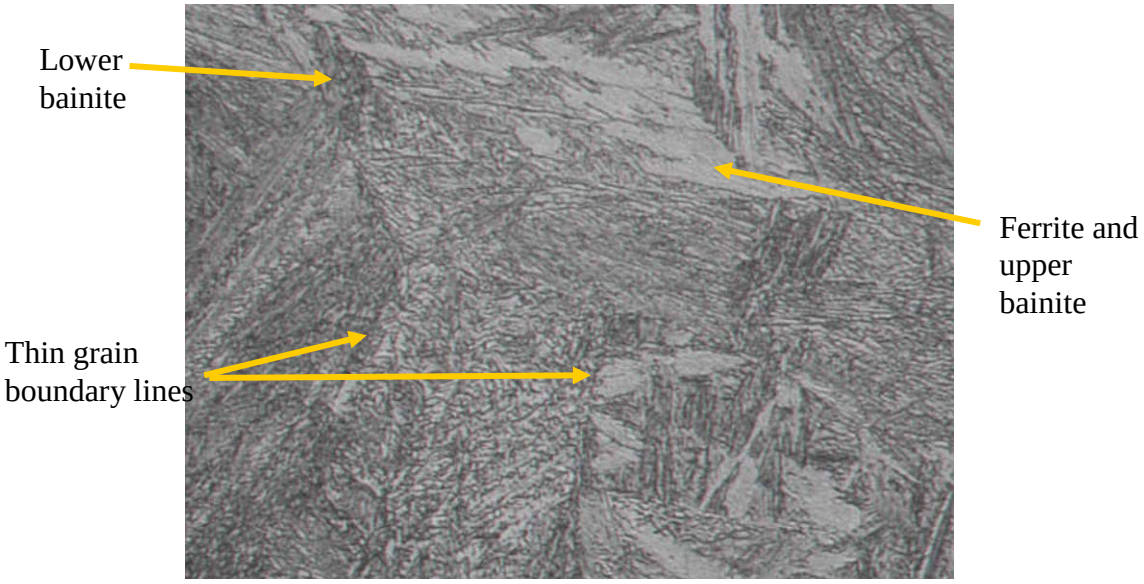

Figure 8. Optical Microstructure of the Bainitic Rail Steel at 1,000×

4. Fracture Toughness

4.1 Introduction

Compact tension specimens were subjected to fatigue precracking to introduce a sharp notch for fracture testing. An intended precrack of approximately 2.5 mm was introduced into each specimen to have a target a/W of 0.5. For the purposes of calculation, the actual crack length was measured from the fracture surface following static failure. Observations made during the precracking are as follows:

- All of the pearlitic steel samples precracked in the normal fashion with relatively straight precracks.
- In the bainitic steel, the first attempt at precracking resulted in a crack growing from an angle out of the notch tip. This was attributed to residual stresses at the machined notch tip. The samples were then stress relieved at 850°F for 30 min. The remainder of the samples was precracked in a normal fashion with relatively straight precracks.
- Initially, the manganese samples could not be precracked. This was due to suspected residual stresses in the notch tip as well as blunting, because of the difficulties in machining. Manganese alloys are known for work hardening, and machining would have caused this at the crack tip. Therefore, the manganese steel samples were stress relieved at 850°F for 30 min. After this treatment, precracking was achieved. However, controlling the crack growth proved to be very difficult, and a consistent total crack length was not achieved among the manganese samples.

4.2. Theoretical Considerations

The general expression of stress intensity factor for a compact tension specimen is:

$$K_1 = \frac{P}{B\sqrt{W}} f(\frac{a}{W}) \tag{1}$$

where P is the load, B is the thickness, W is the distance from the center of the loading holes to the edge of the specimen, a is the total crack length (initial plus precrack), and f(a/W) is a geometrical correction factor. The geometrical correction factor, f(a/W), in eq. 1 can be expressed as:

$$f(\frac{a}{W}) = \frac{(2+(\frac{a}{W}))[0.886+4.64(\frac{a}{W})-13.32(\frac{a}{W})^2+14.72(\frac{a}{W})^3-5.6(\frac{a}{W})^4]}{(1-(\frac{a}{W}))^{3/2}} \tag{2}$$

4.3 Fracture Toughness Results

4.3.1 Bainitic Steel

The bainitic steel demonstrated elastic behavior and cleavage fracture; therefore, ASTM Standard E 399 was used for the analysis. The load versus load–point displacement behavior of three specimens is shown in Figure 9. The data for all three samples tested along with their calculated values of K_{Ic}, based on eq. 1 is presented in Table 3. The average value of K_{Ic} was found to be 52 MPa √m.

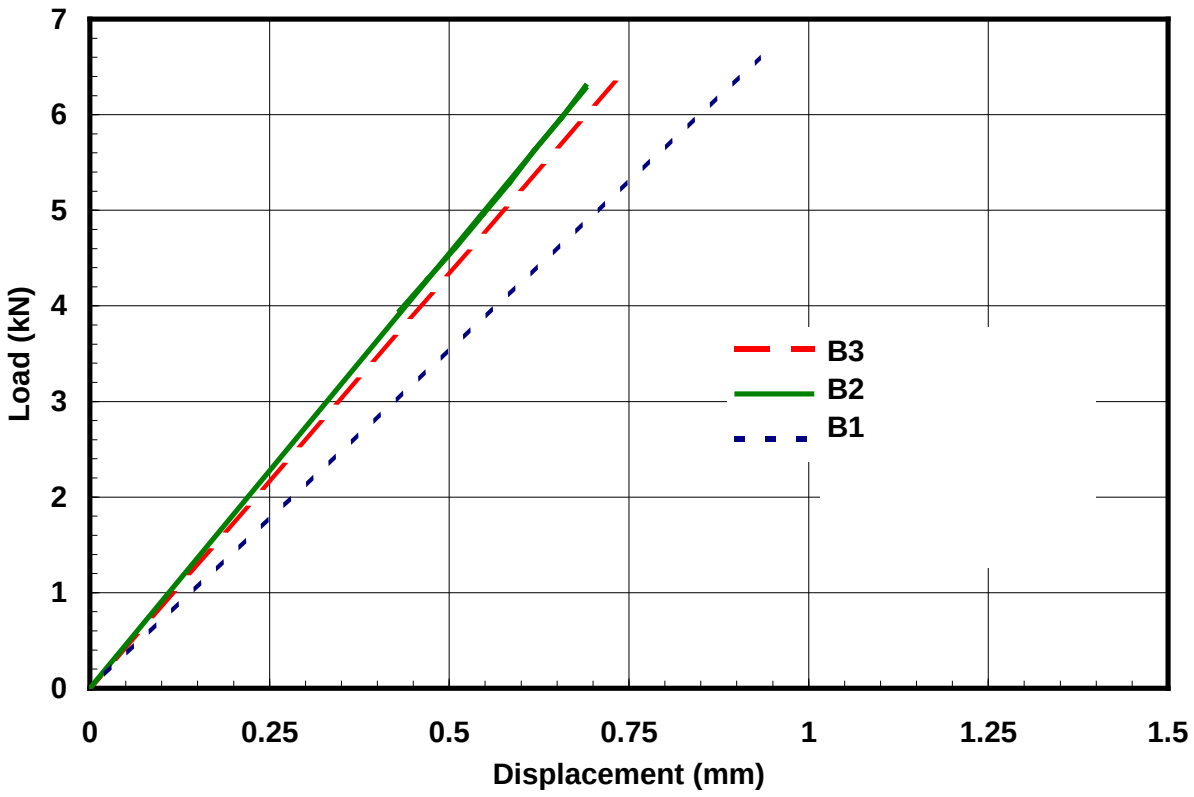

Figure 9. Load vs. Load–Point Displacement Diagram of Three Bainitic (½ T) Compact Tension Specimens

Table 3. Compact Tension Specimen Geometry and Test Results for Bainitic Steel

Sample	W (mm)	a_o (mm)	a_p (mm)	a (mm)	(a/W)	f(a/W)	P_m (kN)	P_q (kN)	B (mm)	Kq (MPa m $^{1/2}$)	K_{Ic} MPa m $^{1/2}$
#1	**22.4**	**8.89**	**3.0**	**11.89**	**0.531**	**10.66**	**6.6**	**6.6**	**9.14**	**51.43**	**51.43**
#2	**22.4**	**8.89**	**3.5**	**12.39**	**0.553**	**11.48**	**6.3**	**6.3**	**9.14**	**52.87**	**52.87**
#3	**22.6**	**8.89**	**3.4**	**12.29**	**0.544**	**11.13**	**6.4**	**6.4**	**9.14**	**51.44**	**51.44**
										Average value of K_{Ic} .	**52**

W = the distance from the center of the loading holes to the edge of the specimen

a_o = initial machined notch length

a_p = fatigue precrack

a = total crack length

P_m = maximum load

P_q = load at which Kq is calculated

B = thickness

K_q = stress intensity factor calculated from eq. 1

K_{Ic} = mode I fracture toughness

To validate the calculated value of K as a true K_{Ic} fracture toughness, the following conditions must be met.

$$a \text{ and } B \geq 2.5 \, (K_Q/\sigma_y)^2 \tag{3}$$

$$P_{max}/P_Q < 1.1 \tag{4}$$

For the bainitic steel, the value of $2.5 \, (K_Q/\sigma_y)^2 = 2.5 \, (52/1{,}100)^2 \times 1{,}000 = 2.24$ mm. This value is less than B, which is 9.14 mm and less than a, which is approximately 12 mm; therefore, the condition of eq. 3 is met. In addition, P_{max} equals P_Q so the condition of eq. 4 is met. Therefore, these fracture tests for the bainitic steel yield a valid value of K_{Ic} according to ASTM E399.

4.3.2 Manganese Steel

The manganese steel demonstrated elastic–plastic behavior with stable ductile crack propagation. The residual strength versus load–point displacement for three specimens is shown in Figure 10. One of the reasons for the difference in the behavior is that these samples all had different precrack lengths, especially sample 2. As discussed earlier, fatigue precracking of manganese steel posed some difficulties in controlling the final target crack length. It can also be seen in Figure 10 that the clearly observed linearity in both the pearlitic and bainitic steels is not displayed here.

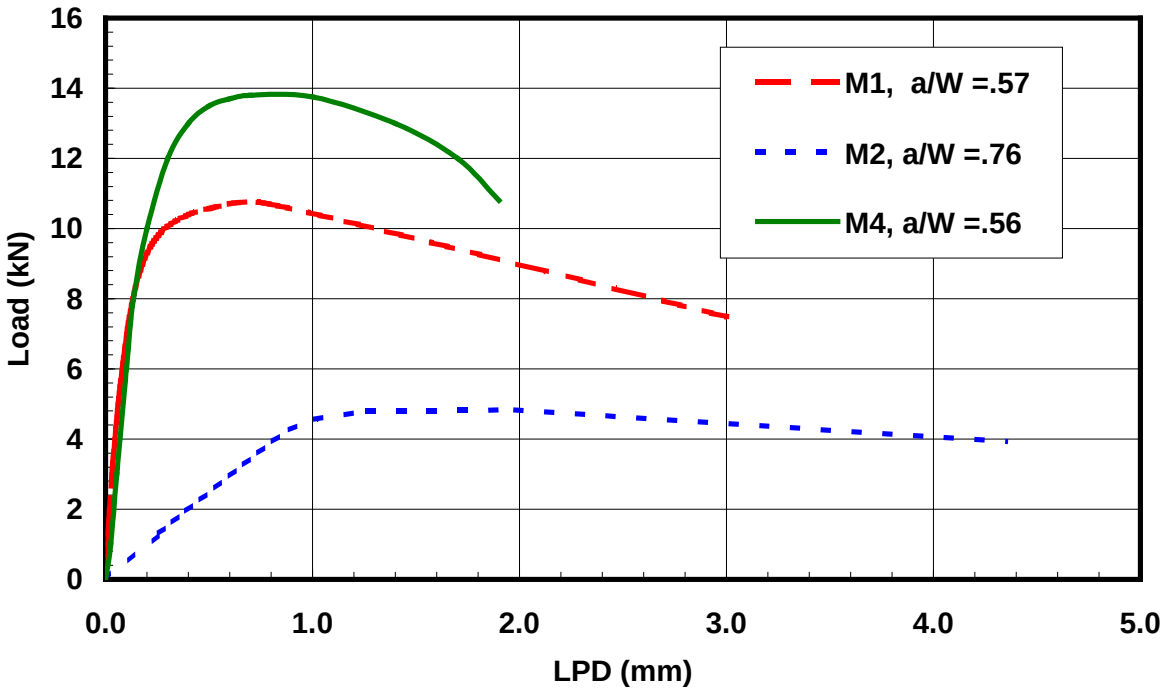

Figure 10. Load vs. Load–Point Displacement Diagram of Three Manganese (½ T) Compact Tension Specimens

Because of the nonlinearity, the value of P_{max}/P_Q in all the manganese specimens is much higher than 1.1. This does not validate one of the requirements for a valid K_{Ic} test according to ASTM standard E399. Nevertheless, a K value was calculated, based on the maximum load sustained by each specimen. These values are given in Table 4 in a similar fashion as given for the pearlitic and bainitic steels. The average K value was used to check the condition, a and $B \geq 2.5 (K_Q/\sigma_y)^2$. For the manganese steel, the value of $2.5 (K_Q/\sigma_y)^2 = 2.5(109/400)^2$ is 185 mm. This also clearly invalidates any calculations based on E399. The full data for the samples tested along with their calculated values is presented in Table 4.

Table 4. Compact Tension Specimen Geometry and Test Results for Manganese Steel

Sample	W (mm)	a_o (mm)	a_p (mm)	a (mm)	(a/W)	f(a/W)	P_m (kN)	P_q (kN)	B (mm)	K_I (MPa m $^{1/2}$)	A (kN-mm)	J_I (kJ/m^2)
#1	22.3	8.89	3.85	12.7	0.571	12.24	10.7		9.14	96	28.0	712
#2	22.4	8.89	8.2	17.1	0.763	31.43	4.8		9.14	110	17.5	766
#3	22.5	8.89	Load was removed after crack jumped, sample was not fractured for future observations.						9.14			
#4	22.4	8.89	3.7	12.6	0.562	11.85	13.8		9.14	120	23.0	572
									Average value	109		683

W = the distance from the center of the loading holes to the edge of the specimen

a_o = initial machined notch length

a_p = fatigue precrack

a = total crack length

P_m = maximum load

P_q = load at which Kq is calculated

B = thickness

K_q = stress intensity factor calculated from eq. 1

K_I = mode I fracture toughness

Energy Release Rate, $J_I = \dfrac{\eta A}{B(W-a)}$

$\eta = 2 + \dfrac{0.522(W-a)}{W}$ for compact tension specimens

A = area under the load vs. displacement curve

To understand the fracture behavior of the manganese steel the fracture toughness J_I was calculated based ASTM E1820-01. This is based on the area under the load–displacement curves in Figure 10. It should be mentioned that the fracture toughness J_I is given as the sum of the elastic and plastic portions.

$$J_I = J_{EL} + J_{PL} \tag{5}$$

From the behavior of the manganese steel, Figure 10, it is reasonable to assume that J_{EL} is very small in comparison with J_{PL}, thus $J \sim J_{PL}$.

$$J_I = J_{PL} = \frac{2\eta}{B(W-a)} \tag{6}$$

The values of J_I for the three manganese samples were calculated and are given in Table 4, as a rough approximation due to the peculiar behavior of this manganese steel. On the basis of this, an average value of J_I of about 680 kJ/m^2 was obtained. This value is similar to that reported for an A285 carbon steel [23, 80].

4.3.3 Pearlitic Steel

The pearlitic steel demonstrated elastic behavior and cleavage fracture; therefore, ASTM Standard E 399 was used for the analysis. The load versus load–point displacement curves can be seen in Figure 11. The data for all three samples along with their calculated values of K_{Ic}, based on eq. 1, is presented in Table 5. The average K_{Ic} value was found to be 41 MPa √m.

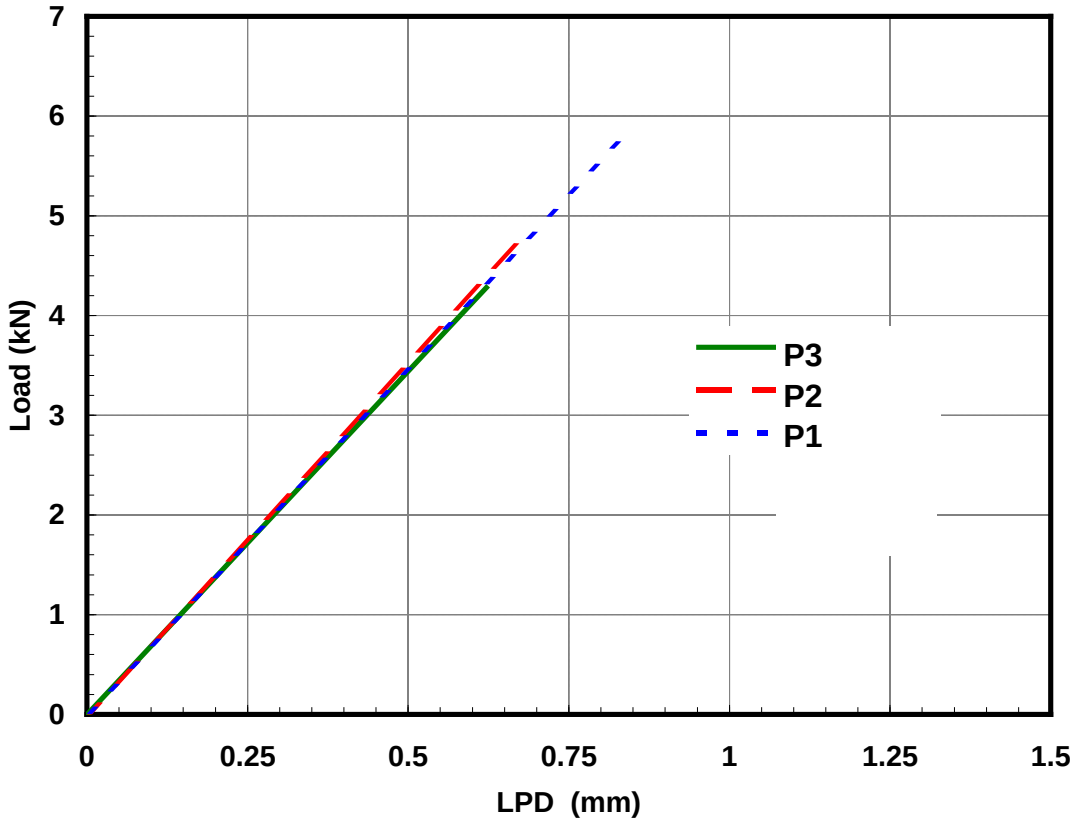

Figure 11. Load vs. Load–Point Displacement Diagram of Three Pearlitic (½ T) Compact Tension Specimens

Table 5. Compact Tension Specimen Geometry and Test Results for Pearlitic Steel

Sample	W (mm)	a_o (mm)	a_p (mm)	a (mm)	(a/W)	f(a/W)	P_m kN	P_q kN	B (mm)	Kq MPa m $^{1/2}$	K_{Ic} MPa m $^{1/2}$
#1	**22.4**	**8.89**	**3.2**	**12.09**	**0.540**	**10.98**	**5.7**	**5.7**	**9.14**	**-**	**45.75**
#2	**22.3**	**8.89**	**3.3**	**12.19**	**0.547**	**11.25**	**4.7**	**4.7**	**9.14**	**-**	**38.74**
#3	**22.4**	**8.89**	**3.7**	**12.19**	**0.562**	**11.85**	**4.3**	**4.3**	**9.14**	**-**	**37.25**
										Average value of K_{Ic} .	**41**
W = the distance from the center of the loading holes to the edge of the specimen a_o = initial machined notch length a_p = fatigue precrack a = total crack length P_m = maximum load P_q = load at which Kq is calculated B = thickness K_q = stress intensity factor calculated from eq. 1 K_{Ic} = mode I fracture toughness											

To validate the calculated value of K as a true K_{Ic} fracture toughness the following conditions must be met.

$$a \text{ and } B \geq 2.5 \, (K_Q/\sigma_y)^2 \tag{7}$$

$$P_{max}/P_Q < 1.1 \tag{8}$$

For the pearlitic steel, the value of $2.5 \, (K_Q/\sigma_y)^2 = 2.5 \, (41/700)^2 \times 1{,}000$ equals 8.6 mm. This value is less than B, which is 9.14 mm and less than a, which is approximately 12 mm; therefore, the condition of eq. 7 is met. In addition, P_{max} equals P_Q, so the condition of eq. 8 is met. Therefore, these fracture tests for the pearlitic steel yield a valid value of K_{Ic} according to ASTM E399.

5. Fatigue Crack Growth

5.1 Introduction

In existing fatigue models, stress dominated crack growth behavior has been considered to describe the FCP kinetics of metallic materials under cyclic loading. Classical FCP laws express cyclic crack extension in terms of some function of the applied load or stress field in the region near the crack tip. Parameters such as the stress intensity factor, the stress intensity factor range, and the energy release rate are commonly used as correlative tools. The equation proposed by Paris and Erdogan [81] has gained the widest acceptance. In this law, the crack growth rate is related to the stress intensity factor range, which can be expressed as:

$$\frac{da}{dN} = A(\Delta K)^m \quad \text{.....(9)}$$

where a is the crack length, N is the corresponding number of cycles, *A* and *m* are parameters that depend on the material properties, and ΔK is the stress intensity factor range. The Paris law is valid for describing the commonly observed linearity of the FCP rate within the stable crack propagation region. The remaining problem of how to predict FCP rates at both low and high values of the stress intensity factor has led to the modification of this fatigue model [81–86].

Jeong, Tang, and Orringer [85, 87] have proposed damage-tolerant strategies for rail steels, based on fracture toughness analysis and FCP kinetics. In their approach, stress intensity factor consideration was applied first to determine the critical defect sizes of detail fracture in rails. Then, a modified Paris equation was used for calculating the time for a detail fracture to grow from a given size to the critical size at which rail failure occurs. The stress intensity factor was calculated using the following formula [87].

$$K_I(a,T) = \frac{2}{\pi}.M_s(\frac{b}{a}).M_1(a).[\sigma_R(a) + \sigma_T(a,T) + M_G(a).\sigma_B(a)].\sqrt{\pi a} \quad \text{.....} \quad (10)$$

where the defect size, *a*, is expressed in terms of the semimajor axis length of an elliptical flaw, M_s stands for the elliptical shape factor of the defect, M_1 accounts for the boundary condition of the defect, M_G reflects the local stress gradients, σ_R is the residual stress, σ_T is the thermal stress, and σ_B is the stress from the bending of the rail. The growth of the crack was assumed to obey the following modified Paris law as proposed by Walker [86]:

$$\frac{da}{dN} = A\frac{(\Delta K)^m}{(1-R)^n} \quad \text{.....} \quad (11)$$

where *R* is the ratio of the minimum to maximum stress, *n* is an empirical constant. Under a simplified loading spectrum, assuming the four wheel loads produce five stress cycles (five pairs of minimum and maximum stresses), the safe-growth time, *N*, for a defect to propagate from an initial defect length to the critical length can be calculated from the following [87]:

$$N = \int_{a_o}^{a_c} \frac{1}{A.\sum_{i=1}^{5} \frac{[\Delta\sigma^{(i)}(a,T)]^m}{[1-R^{(i)}(a,T)]^n}} * \frac{da}{[F(a).\sqrt{a}]^m} \quad \text{.....} \quad (12)$$

where a_o is the initial crack length, a_c is the critical crack length, and *F(a)* is a geometrical function that depends on the defect configuration. It can be expressed as:

$$F(a) = \frac{2}{\sqrt{\pi}}.M_S(\frac{b}{a}).M_1(a) \quad \text{..... (13)}$$

The determination of the stress intensity factor range in the above approach is considerably complex, and the calculation of the integral is also very difficult. Furthermore, the defect size and shape are highly irregular in actual cases. Considering the inaccuracy of field measurement of the defect size, the calculated safe-growth lifetime may vary by several orders of magnitude. The risk of rail failure becomes very difficult to be predicted.

5.2 Results and Discussion

In the current fatigue studies, the maximum fatigue stress used was 200 MPa for the bainitic and pearlitic materials. The rationale was based on approximately 40 percent of the yield strength of the pearlitic steel. The value of 40 percent represents a design safety factor of 2.5. A maximum stress of 97 MPa was used for the fatigue testing of manganese steel. This was calculated based on 20 percent of the maximum stress of the manganese steel.

5.2.1 Fatigue Crack Growth Rates

The average crack length, a, versus the number of cycles, N, for the bainitic, manganese, and pearlitic rail steel is shown in Figure 12. It can be seen from Figure 12 that the total fatigue lifetime of the bainitic steel is much higher than that of the pearlitic steel. This is based on the average of three macroscopically identical specimens from each material. The total average fatigue lifetime for the bainitic steel is approximately 78,000 cycles, while that for pearlitic is approximately 11,000. The fatigue lifetime of manganese steel is approximately 79,000, which is slightly higher than that of the bainitic steel. This difference can be explained by a much smaller maximum load applied to the manganese steel, which is approximately 50 percent less than the bainitic and pearlitic. It is also shown that both initiation lifetime and propagation lifetime for the bainitic steel is higher than that for the pearlitic. Although direct comparison between the lifetime of manganese steel and both bainitic and pearlitic cannot be made here, the data will be compared later on a normalized plot of FCP kinetics and energy release rate.

The slopes of the curves in Figure 12 are taken as the average crack growth rate at each crack length. The relationships between the crack growth rate, da/dN, and crack length, a, for all three rail steels are shown in Figure 13. The curves shown in this figure demonstrate crack growth kinetics of a sigmoidal feature, which can be divided into three stages. The first stage is the crack initiation or the threshold. In the second stage, a stable crack is observed. The curve approached asymptotic values in the third stage (critical stage). In all three stages, the crack growth rate varied. It is obvious that the bainitic rail steel displays a slower crack growth rate at any crack length than the other two rail steels. At stage I the crack growth rate of manganese steel was almost the same as pearlitic steel and much higher than bainitic steel. As the crack length is increased, as can be seen in stage II of Figure 13, the crack growth rate of manganese is decreased, and by the end of stage II and in stage III, the crack growth rate of manganese is close to that of bainitic steel and is much lower than that of pearlitic steel.

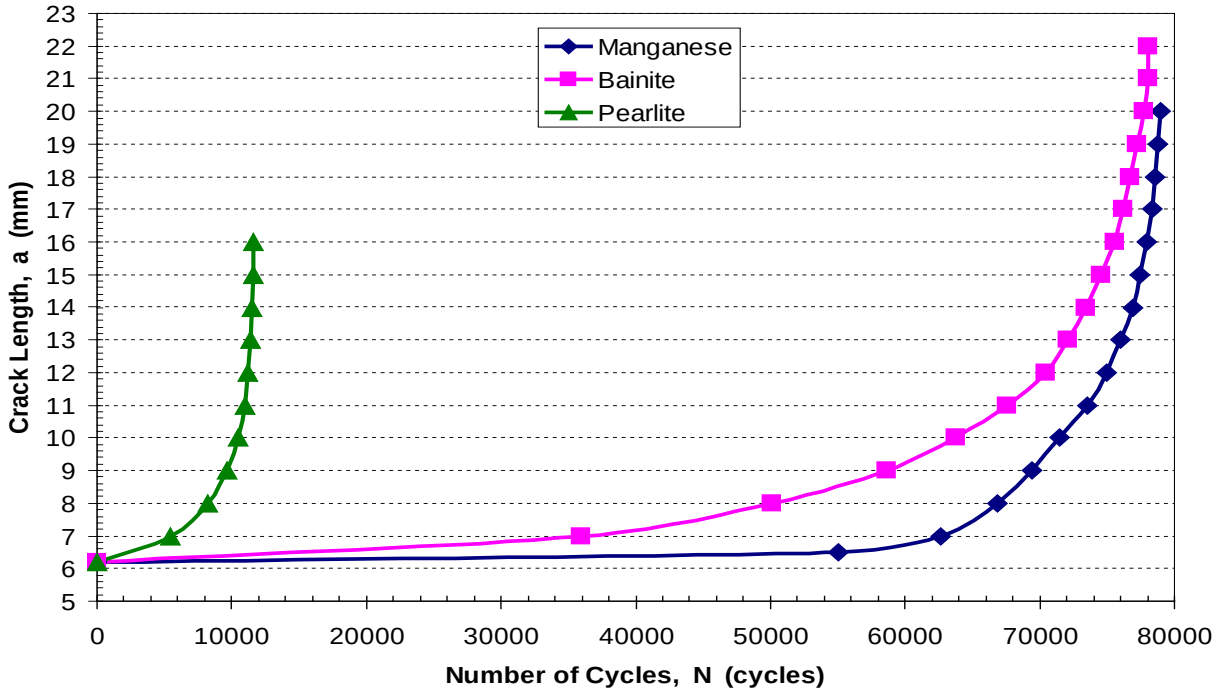

Figure 12. Fatigue Crack Length, a, vs. the Number of Cycles, N

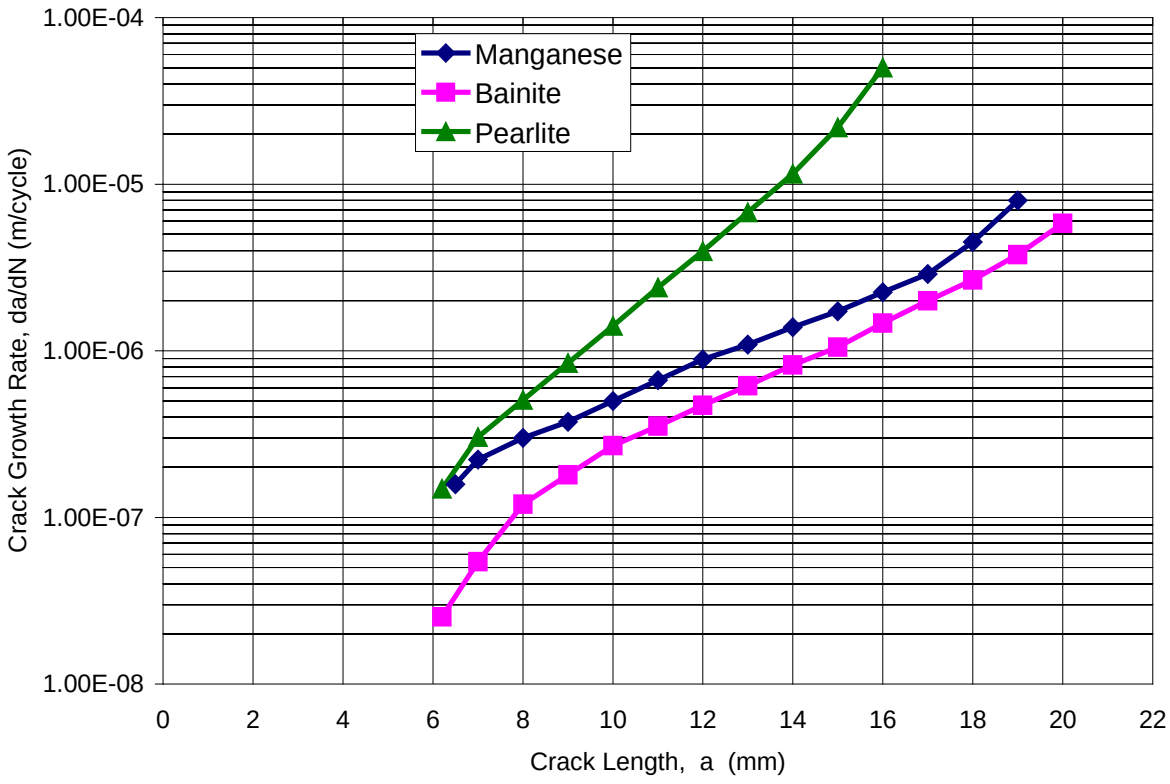

Figure 13. Fatigue Crack Growth Rate, da/dN vs. Crack Length, a

5.2.2 The Potential Energy and the Energy Release Rate

The potential energy, P, was calculated from the hysteresis loops recorded at intervals of number of cycles. It is the area above the unloading curve at each crack length. On this basis, the relationship between the potential energy and the fatigue crack length, a, was established. Figure 14 shows the calculated results of the potential energy of the bainitic, manganese, and the pearlitic steel specimens. It can be seen from Figure 14 that the potential energy, at the critical crack length of the bainitic steel, is higher than that of the manganese and pearlitic steel. It is 1.35 J for the bainitic steel, 0.95 J for manganese steel, and 0.8 J for the pearlitic steel. Also, from the graph, it can be seen that there is a significant difference between the pearlitic steel when compared with the manganese and the bainitic steel.

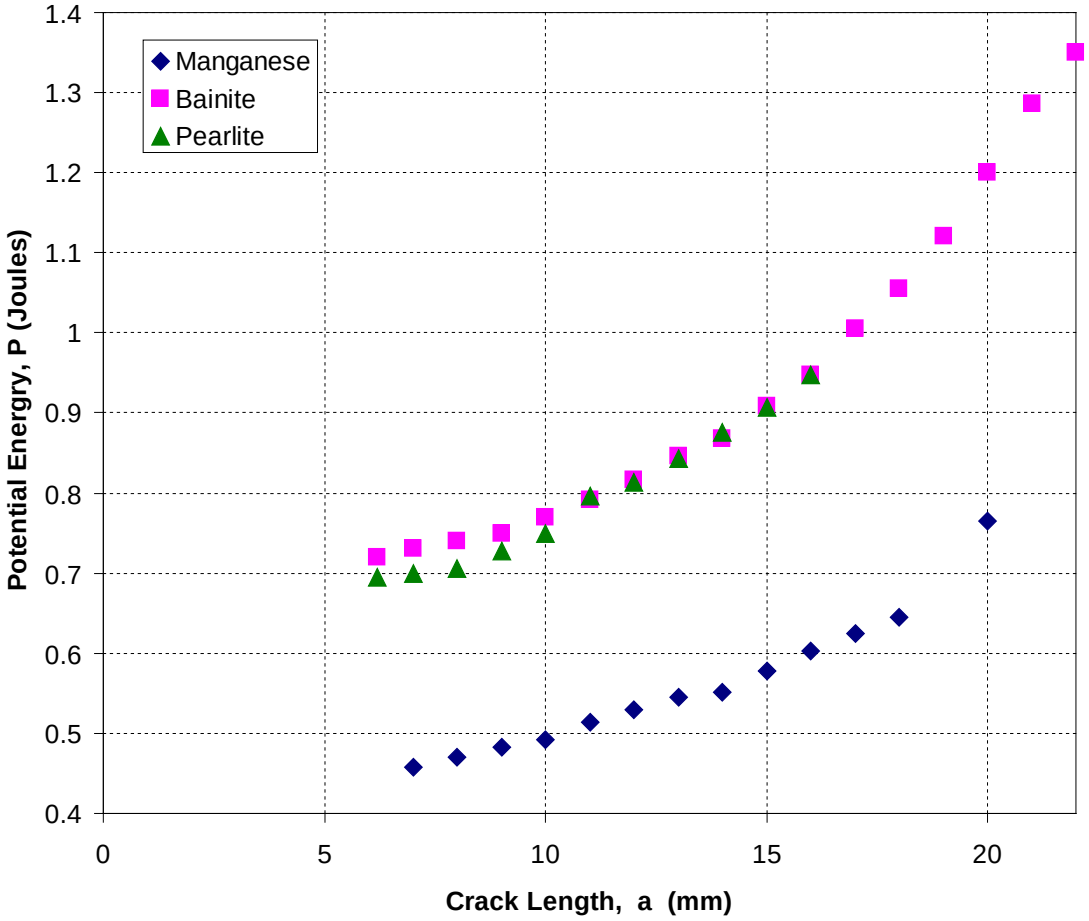

Figure 14. Potential Energy, P, vs. Crack Length, a

The relationship between the potential energy and the fatigue crack length was used to determine the energy release rate J* based on the following equation:

$$J^* = \frac{1}{B}\frac{\partial P}{\partial a} \quad \ldots\ldots\ldots\ldots\ldots\ldots\ldots\ldots\ldots\ldots\ldots\ldots\ldots\ldots \quad (14)$$

where P is the potential energy, a is the crack length, and B is the specimen thickness. Figure 15 illustrates the average energy release rate, J*, as a function of the crack length, a, for the bainitic, manganese, and pearlitic rail steels. The value of J* increases with increasing crack length, a. The critical value of J* for the bainitic steel is approximately 40 kJ/m^2, whereas that of manganese is approximately 36 kJ/m^2 and for the pearlitic steel is approximately 13 kJ/m^2. The ratio between the critical crack length and specimen width ($\frac{a_c}{W}$) is higher for bainitic and manganese steels than that for pearlitic steel. The value of $\frac{a_c}{W}$ is approximately 0.8 for both bainitic and manganese steels and 0.63 and pearlitic steel.

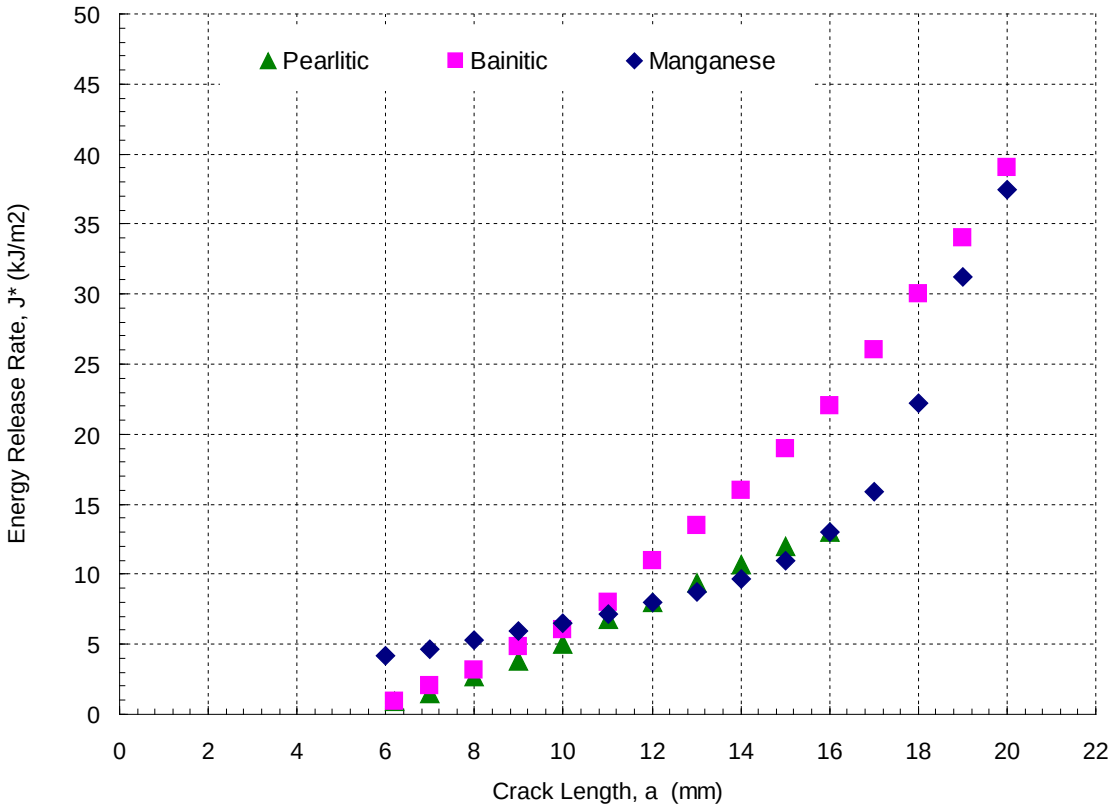

Figure 15. Energy Release Rate, J*, vs. the Fatigue Crack Length, a

5.2.3 FCP Kinetics

The crack growth rate versus the energy release rate J* for bainitic, manganese, and pearlitic rail steel are shown in Figure 16. The crack deceleration in the case of the bainitic and manganese rail steel started after a value of J* of approximately 10 kJ/m^2. This is indicative of material damage ahead of the crack tip. It can also be seen from Figure 16 that the first stage of FCP kinetics is well developed in the bainitic and manganese steel, while that for the pearlitic is less pronounced. Under the same J*, the crack growth rate of pearlitic steel is higher than that of bainitic and lower than manganese steel, which means that bainitic rail steel has highest resistance to FCP in stage I.

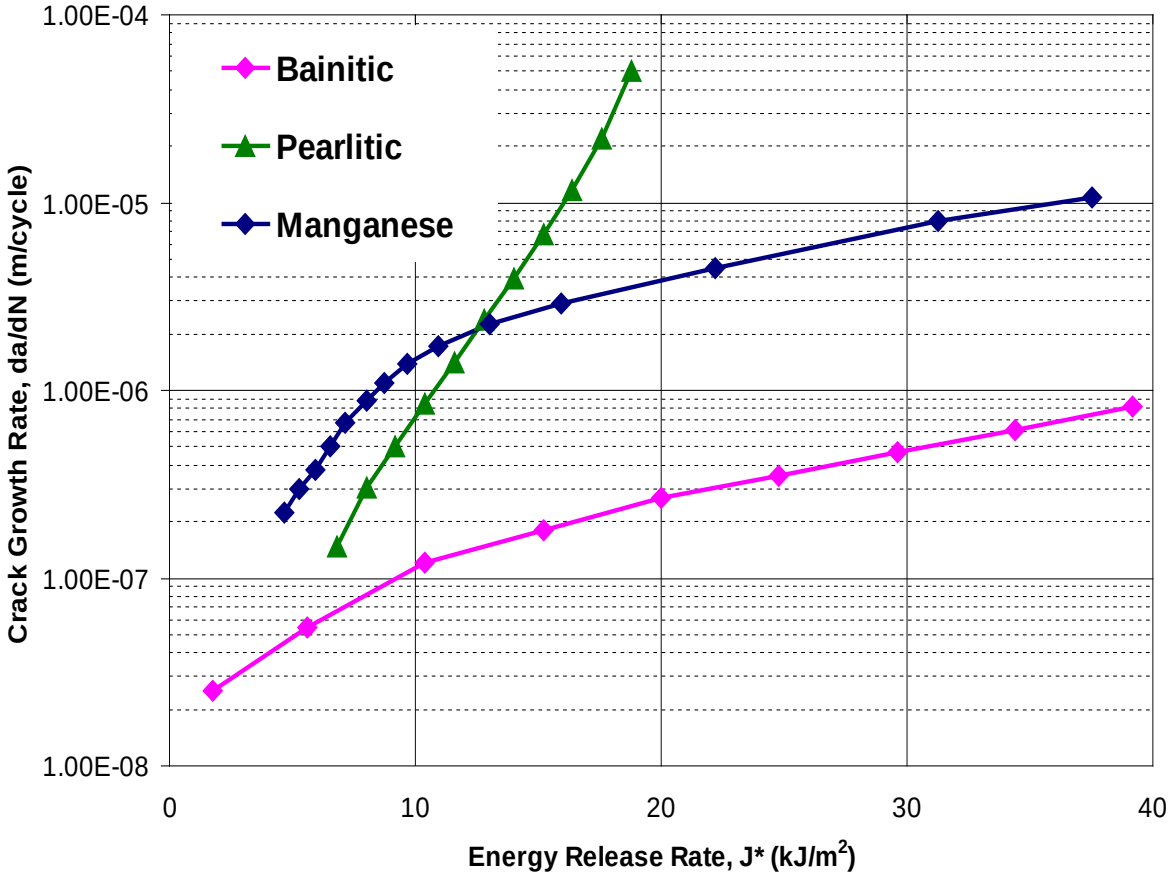

Figure 16. Crack Growth Rate, da/dN, vs. Energy Release Rate, J*

The second stage of FCP kinetics is also different in all three materials. The bainitic and manganese steels exhibit approximately the same rate of change in crack growth rate. These steel samples have a higher rate of change in crack growth rate than that of pearlitic steel as indicated by the lower slope of the curves in Figure 16. The pearlitic steel, does not exhibit such a change in crack growth rate and a clear transition from the first to the second stage of crack propagation kinetics is not shown. It is the second stage of FCP that determines the resistance to FCP of the material. During this stage, for corresponding values of J*, the manganese steel has a significantly higher crack growth rate than that of bainitic steel. Also, the bainitic and manganese steels dissipate about the same amount of energy, which is more energy than that of the pearlitic steel. This takes more energy from the fracture process and thus reduces the crack growth rate. Fracture surface analysis of fatigue-failed specimens should reveal the mechanisms by which the bainitic steel acquires its superior resistance to fatigue crack growth.

In the third stage (unstable crack propagation), the pearlitic steel displays an approximate asymptotic behavior. This indicates an avalanche like fracture after the second stage. The bainitic and manganese steel, however, shows a more gradual transition, which indicates a graceful failure-like behavior.

To calculate the Paris law constants, A and m as given in eq. 9, it is necessary to first substitute J* for K and take the log of both sides. This results in eq. 15.

$$\log\left(\frac{da}{dN}\right) = \log A + m\log(J^*) \tag{15}$$

The data in Figure 16 for the bainitic and pearlitic rail steels is plotted in Figure 17 in the form of eq. 15 to obtain the values of A and m. The average values of A and m for the two materials are given in Table 6. As can be seen, m for the bainitic steel is slightly lower than the manganese steel, but it is approximately one-fifth of the value for the pearlitic steel. The value of A for the bainitic steel is almost the same for manganese steel, and both steels are over 3,000 times greater than that of the pearlitic steel. However, the influence of the value of m in the above equation is much greater than the influence of the constant A because of its role as an exponent rather than as a multiplicative factor. The lower value of m reflects the considerably lower crack growth rates at the same value of J* for the bainitic steel and manganese, even with the much higher value of A.

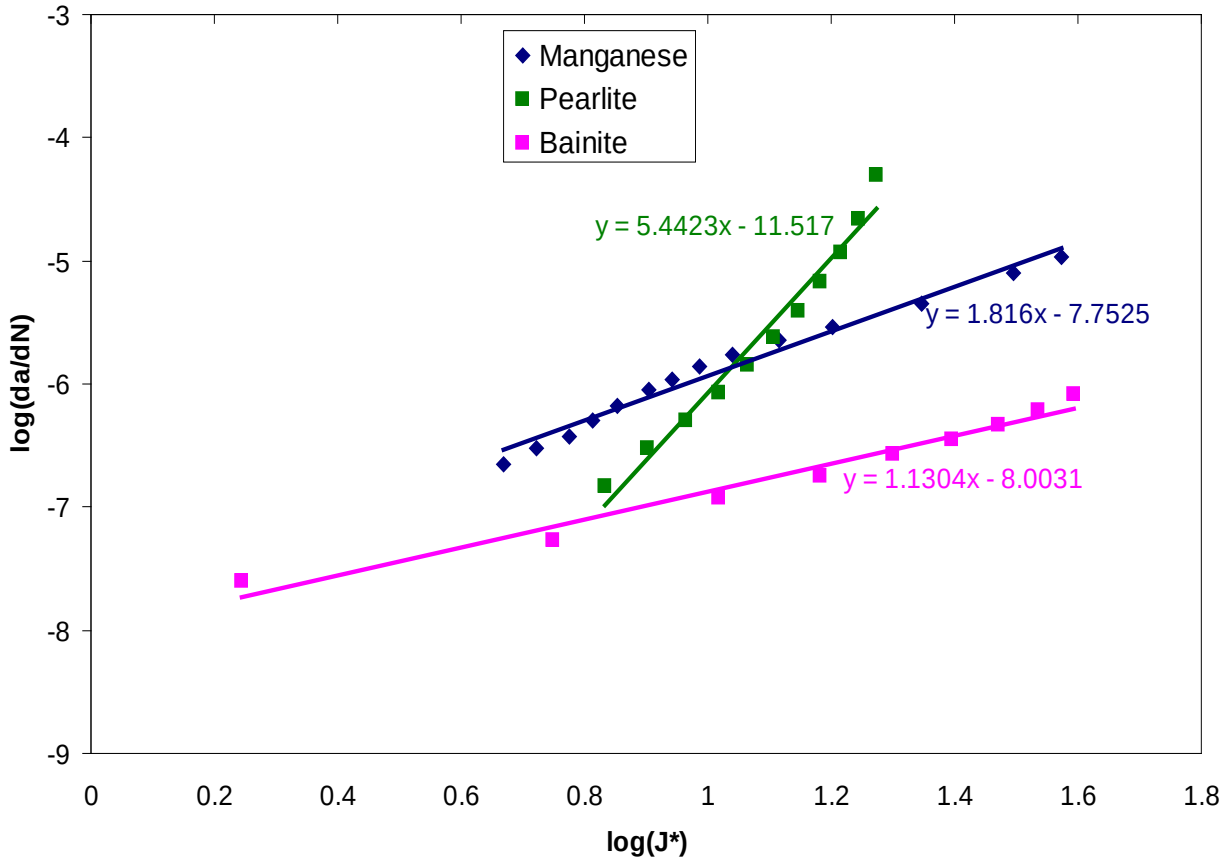

Figure 17. Logarithmic Plot of the Paris Law for the Bainitic, Manganese, and Pearlitic Rail Steels

Table 6. Average Values of Paris Law Constants

Material	A	m
Bainitic rail steel	1.0×10^{-8}	1.13
Pearlitic rail steel	3.04×10^{-12}	5.44
Manganese	1.68×10^{-8}	1.82

5.2.4 Fatigue Fracture Surface Morphology

Fracture surface morphology examination was performed on typical fatigue-failed specimens of each material to identify the fatigue damage species. The fracture surface can mainly be divided into two regions according to the morphological features. Region I is the stable crack propagation region, which contains stages I and II in the FCP kinetics. Region II represents the unstable crack propagation process, which represents stage III of the FCP kinetics. It should be mentioned that differentiating stages I from II is difficult since both are stable events and stage I is normally associated with a very short crack.

Micrographs (300×) taken from the stable crack propagation region, ahead of the notch tip, are shown in Figure 18 to Figure 23 for the bainitic, manganese, and pearlitic rail steels, respectively. Ductile tearing and extensive disoriented ridge formation are associated with the bainitic steel (Figure 18). Ductile flow-like tearing in the direction of crack propagation with feather-like pattern is observed on the fatigue fracture surface of the manganese steel (Figure 19). Pulled-up pearlite lamella, limited microcracks, and microvoid coalescence can be found in the pearlitic steel (Figure 20). In general, these features reflect the crack deceleration and indicate a considerably high-energy–consuming process associated with the crack propagation. It appears to be the case that the bainitic rail steel displays a greater number of randomly oriented ductile fracture features in the first region than the manganese or pearlitic steels. As it was stated earlier, the creation of these fracture species consumes more energy and therefore reduces the crack growth rate in the stable crack propagation region of the bainitic steel.

The unstable crack propagation region was also examined using SEM. At 1,000×, the bainitic steel (Figure 21) exhibits both large and small dimples, indicative of high resistance to material separation. The manganese steel, however, shows a limited number of dimples compared with the bainitic steel. Evidence of oriented tearing flow lines and ridges are apparent on its fracture surface at this high magnification (Figure 22). In contrast, cleavage and intergranular separation are associated with the fast crack region in the pearlitic steel (Figure 23). It is obvious from the fracture surface morphological features displayed in these micrographs that the bainitic rail steel offers more resistance to material separation than the manganese or pearlitic rail steels. Manganese displays more ductile features than the pearlitic steel, indicative of its superior fatigue separation performance to pearlitic.

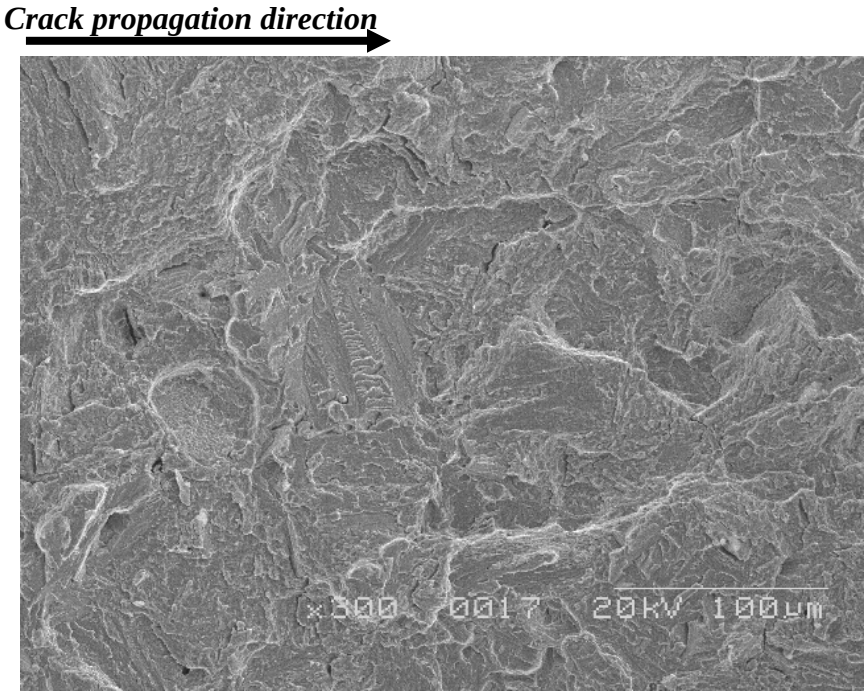

Figure 18. An SEM Micrograph at 300× Taken from the Beginning of the Stable Crack Propagation Region of the Bainitic Rail Steel (Ductile fracture mechanisms characterized by extensive tearing and ridge formation are seen.)

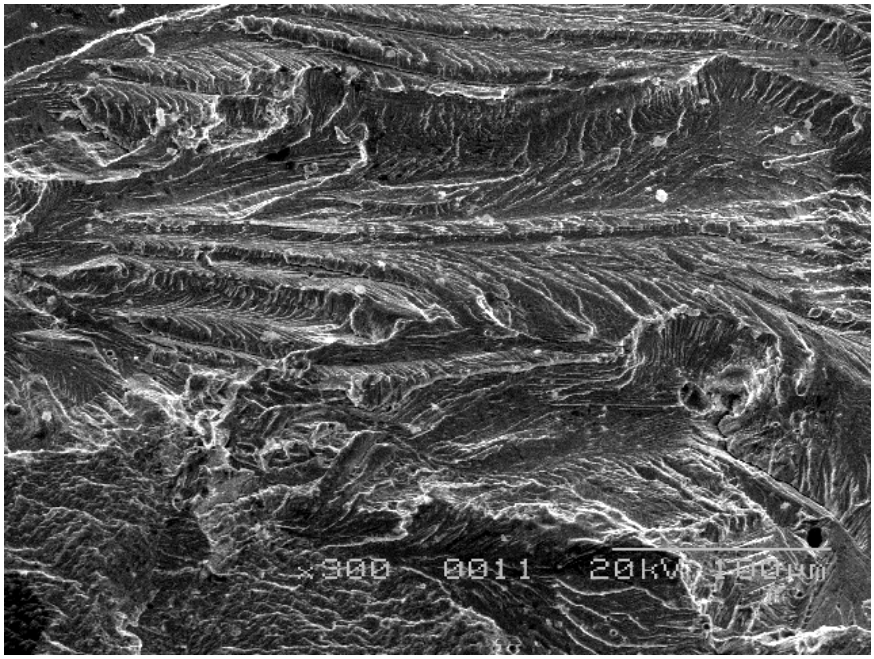

Figure 19. An SEM Micrograph at 300× Taken from the Beginning of the Stable Crack Propagation Region of the Manganese Rail Steel (Ductile flow-like tearing in the direction of crack propagation. This produces an extended feather looking pattern seen at 300×.)

Crack propagation direction

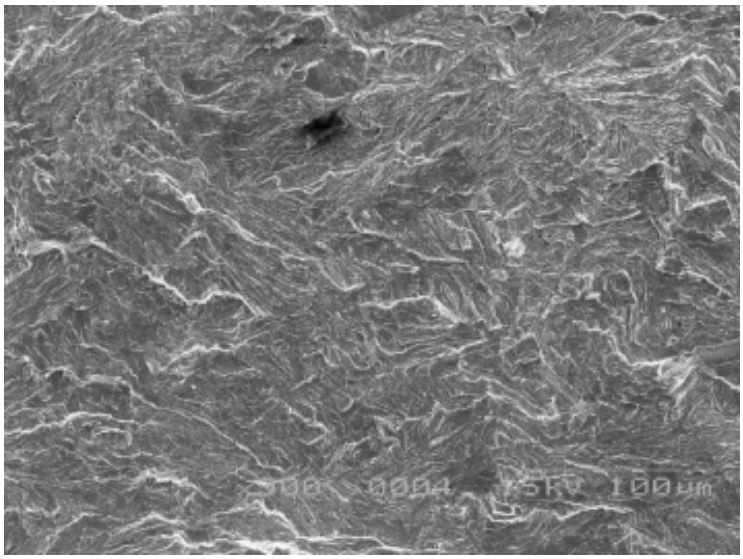

Figure 20. An SEM Micrograph at 300× Taken from the Beginning of the Stable Crack Propagation Region of the Pearlitic Rail Steel, Showing a Ductile Fracture Mechanism Characterized by Ductile Tearing, Pulled-Up Pearlite Lamella and Limited Microvoids Coalescence

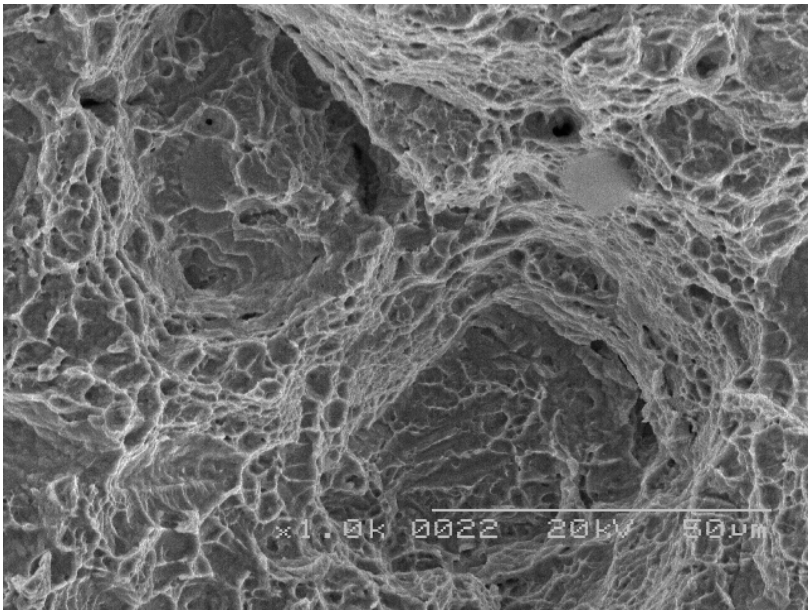

Figure 21. An SEM Micrograph at 1,000× Taken from the Middle of the Fast Crack Propagation Region for the Bainitic Rail Steel (Clear ductile fracture dimples and dense tearing ridges are seen.)

Crack propagation direction

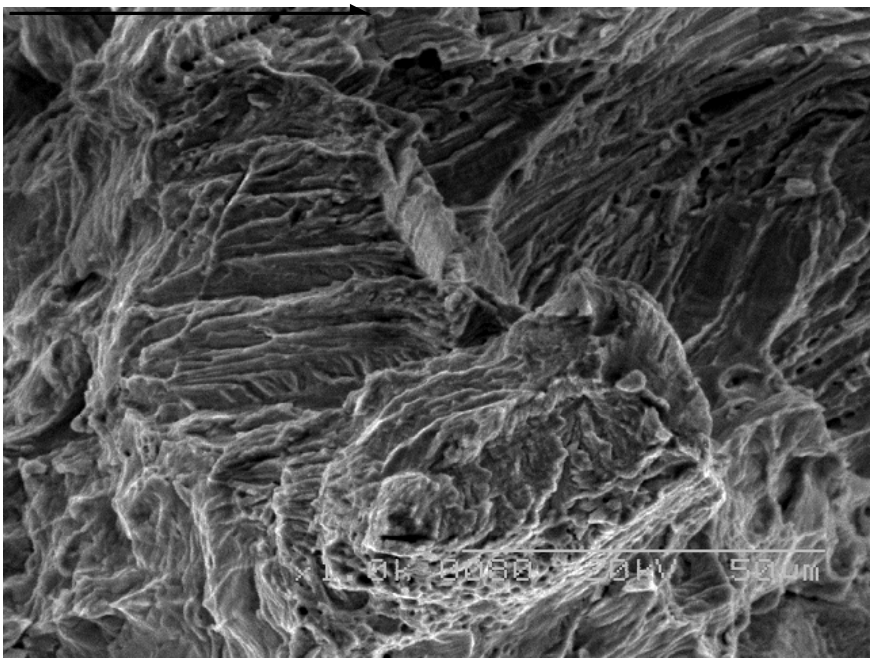

Figure 22. An SEM Micrograph at 1,000× Taken from the Middle of the Fast Crack Propagation Region for the Manganese Rail Steel Showing a Limited Number of Dimples, Oriented Tearing Flow Lines, and Ridges

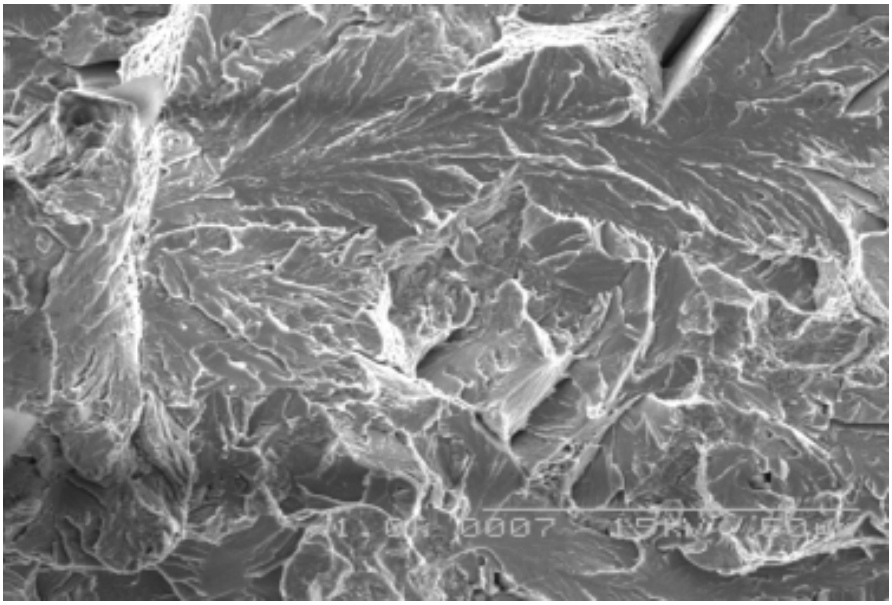

Figure 23. An SEM Micrograph at 1,000× Taken from the Middle of the Fast Crack Propagation Region for the Pearlitic Rail Steel, Showing Ridges, Pits, and Crevices along the Grain Boundaries Indicative of Quasi-Brittle Fatigue Failure

6. Hardness, Fracture Toughness and Fatigue Damage Relationship

6.1 Introduction

All three samples (pearlitic, bainitic, and manganese) were tested for their hardness. A total of five tests were done on each sample and the average of the tests was recorded. The hardness tester used was the Time TH150 Hardness Tester, which was developed by Dr. Leeb. This type of tester is known as a scleroscope, it measures the height of rebound of an indenter dropped onto a material. In details, the indenter is dropped on the material being tested and the impact and rebound velocity is measured when the indenter is 1 mm above the surface. The Leeb number is then calculated by taking the ratio of the rebound velocity to the impact velocity.

$$HL = \frac{1000V_b}{V_a} \tag{16}$$

where V_b and V_a are the rebound and impact velocity, respectively. The same instrument is capable and was used to measure the Brinell and the Vickers number.

6.2 Results and Discussion

The results obtained from the test are shown in the Table 7. For the Leeb Hardness test (HLC), it can be seen that the bainitic rail steel has the highest value of 611, followed by the pearlitic rail steel with a value of 549, and then the manganese with value of 357. Both the Brinell hardness (HB) test and Vickers hardness (HV) test shows a similar trend in the hardness of the materials. It can also be seen that the Brinell and Vickers test have hardness values that are very similar.

Table 7. Hardness Number for Leeb, Brinell, and Vickers Tests

Test Method / Materials	(Leeb Test) HLC	(Brinell Test) HB	Vickers Test (HV)
Bainitic Rail Steel	611	290	299
Pearlitic Rail Steel	549	199	201
Manganese	357	93	90

6.2.1 Hardness Comparison to Stress–Strain Relationship

The hardness can be compared with the stress–strain curves of the specific material to gain a better understanding of the properties of the materials. The stress–strain diagram of the bainitic, pearlitic, and manganese rail steel is shown in Figure 4, with the corresponding yield strength, ultimate strength, and failure strain percent in Table 2. As shown in the stress–strain diagram (Figure 4), the bainitic rail steel has the highest yield strength, ultimate strength, and failure strain, followed by the pearlitic then the manganese. This trend is similar to that of the hardness test, which shows that the hardness of the material plays an important role in the yield and

ultimate strength of a material. The bainitic rail steel has the smallest grain size and the highest hardness number, and manganese rail steel has the largest grain size and the smallest hardness number. The pearlitic rail steel, in contrast, had both a grain size and a hardness number that fell between the bainitic and manganese rail steel. This shows that as the grain size decreases the hardness increases, which is also known as the Hall–Petch effect.

6.2.2 Hardness Comparison to Fracture Toughness

When the hardness number to the fracture toughness of the rail steels is compared, it can be seen that there is a similar trend between bainitic rail steel and pearlitic rail steel. The hardness number is higher for bainitic rail steel than for the pearlitic rail steel; these results are shown in Table 7. The same trend is seen for the fracture toughness of bainitic and pearlitic rail steel that has an elastic behavior. When the ASTM standard E399 is used, the fracture toughness of bainitic rail steel was found to be 52 MPa √m and that of pearlitic rail steel was 41 MPa √m; these data can be seen in Table 7 and Table 5, respectively. As for the manganese steel, a severe nonlinearity does not validate one of the requirements for a valid K_{Ic} test according to ASTM standard E399; therefore, ASTM standard E1820-01 was used. On this basis of E1820-01, a value of the energy release rate J was calculated. The manganese rail steel under consideration displays a dominant plastic deformation, although it is lower than that of the bainitic and pearlitic rail steels. Thus, there is no correlation between hardness and fracture toughness when the material displays considerable plastic deformation.

6.2.3 Hardness Comparison to Fatigue Crack Growth

There is no clear relationship between the hardness and the fatigue crack growth of the different rail steels. However, from Table 7, it is seen that the bainitic steel has the highest hardness, and from Table 6, it has the smallest Paris Law constant m, and its Paris Law constant A is between pearlitic and manganese. Although manganese has the lowest hardness number, its Paris Law constant m is between that of bainitic and pearlitic rail steel, and it has the highest Paris Law constant A. As for the pearlitic steel, its hardness is between that of bainitic and manganese steel, but it has the largest Paris Law constant m and the smallest Paris Law constant A. The influence of the Paris Law constant m has a much greater influence than the constant A because of its role as an exponent rather than as a multiplicative factor. On the basis of the current study, it appears that there is no direct correlation between hardness and the fatigue crack growth behavior of rail steels.

7. Concluding Remarks

The bainitic rail steel has the highest mechanical properties as compared to AMS and pearlitic rail steels. Examination of the microstructural features reveals that bainitic steel has a more intricate structure than AMS and pearlitic. AMS shows very few signs of being work hardened or toughened, which usually increases the mechanical properties of the material. As the number of alloying elements increase, the microstructure of the steel becomes more complex, resulting in the increase of mechanical properties and fracture toughness.

To further investigate the fracture toughness, fracture mechanics tests were conducted on three steels, namely pearlitic, bainitic and manganese using a (½ T) compact tension specimens. At least three specimens from each material were tested. It is concluded that:

- The pearlitic steel obeyed the linear elastic fracture mechanics theory with an average K_{Ic} of 41 MPa √m, based on ASTM standard E399.
- The bainitic steel obeyed the linear elastic fracture mechanics theory with an average K_{Ic} of 52 MPa √m, based on ASTM standard E399.
- The manganese steel behaved in an elastic plastic manner with dominant plastic deformation. ASTM standard E399 could not be invoked because of such behavior. Therefore, ASTM standard E1820-01 was used to determine an approximate value of the energy release rate J_I for the manganese steel. This average value was found to be 680 kJ/m^2. Difficulties were encountered in both machining and fatigue precracking the manganese compact tension specimens. This has caused residual stresses that have affected the procedures for producing a consistent initial fatigue precrack.

The fatigue behavior was investigated by performing FCP analysis of J6 bainitic, manganese, and pearlitic rail steels. It was found that the bainitic rail steel has the highest initiation and propagation lifetimes, followed by the manganese steel then the pearlitic steel. The average total fatigue lifetime of the bainitic steel specimens is approximately seven times that for the pearlitic, tested under the same conditions. The critical value of the energy release rate J*, obtained from the hysteresis loops during fatigue testing, was found to be approximately 40, 36, and approximately 13 kJ/m^2 for the bainitic, manganese, and pearlitic rail steels, respectively. This occurred at a critical crack length to specimen width ratio of 0.80 for bainitic and manganese steels and 0.63 for pearlitic steel. It was found that the crack growth rate for the bainitic steel is lower than that of the pearlitic and manganese steel over the entire range of the energy release rate. Stage I for manganese steel showed a higher crack growth rate than pearlitic steel. In stages II and III the gradient of the crack growth rate decreased significantly for the manganese steel and was much lower than that of the pearlitic steel. The bainitic and manganese steel exhibits a higher rate of decelerating the crack growth rate in the second stage, as indicated by the lower slope of the FCP curve in comparison with the pearlitic steel. The fatigue crack growth of the rail steel was expressed in the form of a power law, $(da/dN) = A(J^*)^m$, where A and m are empirical constants. It was found that the value of m for the bainitic and manganese steel was approximately the same and they were about one fifth of the value for the pearlitic steel, reflecting the considerably lower crack growth rate at the same value of J* for the bainitic and manganese steel. This indicates the superior resistance of bainitic and manganese rail steel to FCP (i.e., higher fatigue damage tolerance).

According to the morphological features, the fatigue fracture surface can mainly be divided into two regions. Region I is the stable crack propagation region, which contains stages I and II in the FCP kinetics. Region II represents the unstable crack propagation, which is stage III of FCP kinetics. The bainitic rail steel displays more ductile fracture features in the first region than the pearlitic steel. Ductile tearing and extensive ridge formation are associated with the bainitic steel in this region. These features reflect the crack deceleration and indicate a considerably high energy consuming process associated with the crack propagation of the bainitic steel. Pulled-up pearlite lamella, limited microcracks and microvoid coalescence were found on the fracture surface of the pearlitic rail steel in the first region. The unstable crack propagation region of the bainitic steel exhibits both large and small dimples indicative of high resistance to material separation. In contrast, cleavage and intergranular separation are associated with the fast crack region in the pearlitic rail steel.

In regard to the relationship between hardness, fracture toughness and fatigue crack growth behavior, it has been concluded that:

- The bainitic rail steel has the highest hardness number followed by the pearlitic then the manganese rail steel, this is the same trend for the yield strength and ultimate strength.
- The smaller the grain size the higher the hardness number.
- For bainitic and pearlitic rail steel that possess elastic behavior, the higher the fracture toughness of the material the higher the hardness. But for manganese rail steel that has a nonlinear elastic–plastic behavior, the fracture toughness cannot be correlated to the hardness. This is due to the dominant plastic deformation properties of the manganese steel.
- There is no clear relationship between the hardness of the rail steels and fatigue crack growth behavior.

8. References

1. Smith, W. F. (2004). Engineering alloys. In *Foundations of materials science and engineering* (3rd ed.) (pp. 427–522). New York, NY: McGraw Hill.
2. Bayraktar, E., Khalid, F. A., and Levaillant, C. (2004). Deformation and fracture behavior of high manganese austenitic steel. *Journal of Materials Processing Technology*, *47*, 145–154.
3. Aglan, H. A., Liu, Z. Y., Hassan, M. F., and Fateh, M. (2004). Mechanical and fracture behavior of bainitic rail steel. *Journal of Materials Processing Technology*, *151*, 268–274.
4. Key to Metals. (n.d.) Influence of alloying elements on steel microstructure. Accessed June 2005 from: http://www.keytometals.com/articles/art50.htm.
5. Khourshid, A. M., Gan, Y. X., and Aglan, H. A. (2001). Microstructure origin of strength and toughness of a premium rail steel. *Journal of Materials Engineering and Performance*, *10*, 331–336.
6. Davis, J. R. (Ed.). (1998). *Metals handbook, desk edition* (2nd ed.) (pp. 169–170, 1384–1385). Washington, DC: ASM International.
7. Yanushkevich, Z., Mogucheva, A., Tikhonova, M., Belyakov, A., and Kaybishev, R. (2011). Structural strengthening of an austenitic stainless steel subjected to warm-to-hot working. *Material Characterization*, *62*, 432–437.
8. Key to Metals. (n.d.) Austenitic manganese steels. Accessed June 2005 from: http://www.keytometals.com/page.aspx?ID=CheckArticle&LN=EN&site=KTS&NM=69 .
9. Sawley, K. J. (1997). Bainitic steels for rail. *Technology Digest*, TD97-001. Pueblo, CO: Association of American Railroads/Transportation Technology Center, Inc.
10. Sawley, K. J., and Davis, D. (1996). An improved bainitic steel for frogs. *Technology Digest*, TD96-026. Pueblo, CO: Association of American Railroads/Transportation Technology Center, Inc.
11. Hassan, M., Jones, W., Aglan, H., and Fateh, M. (2004 Aug.). Microstructure-properties relationships of bainitic and pearlitic rail steel. In H. Mahfuz and M. V. Hosur (Eds.), Proceedings of the *22nd Southeastern Conference on Theoretical and Applied Mechanics: Developments in theoretical and applied mechanics* (Vol. XXII). Tuskegee, AL: Tuskegee University.
12. Key to Metals. (n.d.) Bainitic steels: Part one. Accessed on June 2005 from: http://www.keytometals.com/page.aspx?ID=CheckArticle&LN=EN&site=KTS&NM=144.
13. Bayraktar, E., Khalid, F. A., and Levaillant, C. (2004). Deformation and fracture behaviour of high manganese austenitic steel. *Journal of Materials Processing Technology*, *147*, 145–154.
14. Su, X., and Clayton, P. (1997). Ratchetting strain experiments with a pearlitic steel

under rolling/sliding contact. *Wear*, *205*, 137–143.

15. Norton, R. L. (1998). *Machine design: An integrated approach*. Upper Saddle River, N.J.: Prentice-Hall.
16. Yokoyama, H., Mitao, S., Yamamoto, S., Kataoka, Y., and Sugiyama, T. (2001). High strength bainitic steel rails for heavy haul railways with superior damage resistance. *NKK Technical Review*, *84*, 44–51.
17. Yokoyama, H., Mitao, S., Yamamoto, S., and Fujikake, M. (2002). Effect of the angle of attack on flaking behavior in pearlitic and bainitic steel rails. *Wear, 253*, 60–66.
18. Broek, D. (1989). *The practical use of fracture mechanics* (pp. 465–476). Dordrecht, The Netherlands: Kluwer Academic Publishers.
19. Rice, R. C., Rungta, R., and Broek, D. (1983). *Post-service rail defect analysis (third interim report*). Prepared by the Battelle Columbus Laboratories (Columbus, OH). Cambridge, MA: John A. Volpe Transportation Systems Center.
20. Orringer, O., Tang, Y. H., Jeong, D. Y., and Perlman, A. B. (1999). *Risk/benefit assessment of delayed action concept for rail inspection* (U.S. Department of Transportation Report No. DOT/FRA/ORD-99/03; DOT-VNTSC-FRA-99-7). Washington, DC: Federal Railroad Administration, Office of Research and Development. http://www.fra.dot.gov/downloads/Research/ord9903.pdf.
21. Orringer, O. (1984). Rapid estimation of spectrum crack-growth life based on the palmgren-miner rule. *Computers and Structures*, *19*, 149–153.
22. Orringer, O., Tang, Y. H., Gordon, J. E., Jeong, D. Y., Morris, J. M., and Perlamn, A. B. (1988). *Crack propagation life of detail crack fractures in rails* (U.S. Department of Transportation Report No. DOT/FRA/ORD-88/13). Washington, DC: Federal Railroad Administration, Office of Research and Development. http://www.volpe.dot.gov/sdd/docs/1988/crackpropagation.pdf.
23. Glowacki, M., and Kuziak, R. (1997). Application of coupled thermal-mechanical model to the numerical analysis of the microstructure development during rolling and air-cooling rails. In D. R. J. Owen et al. (Ed.), Proceedings of the *Fifth International Conference on Computational Plasticity International Conference on Computational Plasticity* [5–7 Sept. 2005, Barcelona, Spain] (Parts 1 and 2, pp. 1313-1316). Swansea, U.K.: Pineridge Press.
24. Wong, S. L., Bold, P. E., Brown, M. W., and Allen, R. J. (1996). A branch criterion for shallow angled rolling contact fatigue cracks in rails. *Wear*, *191*, 45-53.
25. Muster, H., Schmedders, H., Wick, K., and Pradier, H. (1996). Rail rolling contact fatigue: The performance of naturally hard and head-hardened rails in track. *Wear*, *191*, 54-64.
26. Vitez, I., and Todic, B. (1992). Importance of knowing fracture toughness and fatigue strength of railway rails. In S. Sedmak, A. Sedmak, and D. Ruzic (Eds.), Proceedings of the Ninth European Conference on Fracture, *ECF 9 - reliability and structural integrity of advanced materials* [21–25 Sept. 1992, Varna, Bulgaria] (Vols. I and II, pp. 1291-1296). Sheffield, U.K.: EMAS Publishing.

27. Tobias, D. H., and Foutch, D. A. (1995). Reliability-based method for fatigue evaluation of railway bridges. *Journal of Bridge Engineering*, *2*, 231–243.

28. U.S. Department of the Army. (1994). *Hand Receipt Covering Content of Sets, Kits, and Outfits Component List for Railway Construction Set* [microform]. Railroad Track Maintenance and Rehabilitation Equipment (Report No. NSN 2230-00-849-8629, LIN R05441). Washington, DC: U.S. Department of the Army.

29. The board of directors. (1907). *Manual of recommended practice for railway engineering and maintenance-of-way*. Chicago, IL: American Railway Engineering and Maintenance-of-Way Association.

30. Raymond, W. G. (1909). *The elements of railroad engineering*. London, U.K.: John Wiley and Sons.

31. Law, E. H., Hadden, J. A., and Cooperrider, N. K. (1977). *General models for lateral stability analyses of railway freight vehicles* (Report No. U.S. Department of Transportation FRA/ORD-77/36 [interim report]). Springfield, VA: National Technical Information Service.

32. Allen, C. J. (1959). *Modern railways: Their engineering equipment and maintenance* (p. 78). London, U.K.: Faber and Faber Limited.

33. (1980). Remarks on the *Comparative merits of cast metal and malleable iron railways: An account of the Stockton and Darlington Railway, and the Liverpool and Manchester Railway* [microform]. Woodbridge, U.K.: Research Publications.

34. Persad, C., and Raghunathan, S. (1995). Post-test characterization of the hardness and microstructure of copper rails from a 9 MJ electromagnetic launcher. *IEEE Transactions on Magnetics*, *31*, 740-745.

35. Liu, Y. Z. (1997). Experimental investigation of the mechanical properties of quenched rails for different quenching conditions using the temperature directly from rolling heating. *Journal of Materials Processing Technology*, *63*, 542-545.

36. Tratman, E. E. R. (1901). *Railway track and track work*. New York, NY: The Engineering News Publishing Co.

37. Tratman, E. E. R. (1897). *Railway track and track work*. New York, NY: The Engineering News Publishing Co.

38. Rangwala, S. C. (1964). *Principles of railway engineering*. Anand, Gujarat, India: Charotar Book Stall.

39. (1921). *Manual of the American Railway Engineering Association: Definitions, specifications and principles of practice for railway engineering*. Chicago, IL: American Railway Engineering Association.

40. (1915). *Manual of the American Railway Engineering Association*. Chicago, IL: American Railway Engineering Association.

41. Raymond, W. G., Riggs, H. E., and Sadler, W. C. (1937). *The elements of railroad engineering* (p. 95). London, U.K.: John Wiley and Sons.

42. American Railway Engineering and Maintenance-of-Way Association. (1997). *AREMA*

manual for rail engineering (p. 4-2-6). Lanham, MD: American Railway Engineering and Maintenance-of-Way Association.

43. Stone, D. H. (1982). The increasing demands on the serviceability of rail steels. *Canadian Metallurgical Quarterly, 21*, 17–24.

44. Bramwell, S., and McElroy, T. F. (1987). *Heavy haul railway conference proceedings*, Perth, Australia, Paper A.4.

45. Silva, L. D., and Nobrega, M. L. (1987). *Heavy haul railway conference proceedings*, Perth, Australia, Paper I.9.

46. Beynon, J. H., Garnham, J. E., and Sawley, K. J. (1996). Rolling contact fatigue of three pearlitic rail steels. *Wear, 192*, 94-111.

47. Hellier, A. K., and Merati, A. A. (1998). The mode I fatigue threshold for head hardened rail steel. *International Journal of Fatigue, 20*, 247-249.

48. Tyfour, W. R., Beynon, J. H., and Kapoor, A. (1995). The steady state wear behaviour of pearlitic rail steel under dry rolling-sliding contact conditions. *Wear, 180*, 79-89.

49. Singh, U. P., Singh, R., and Banerjee, S. (1995). Fatigue crack growth rate and fracture toughness of rail steels. *Scandinavian Journal of Metallurgy, 24*, 237-241.

50. Vitez, I. (1996). The fracture toughness and the fatigue strength of railway rails. *Metalurgija, 35*, 49-51.

51. Smith, W. F. (1993). *Structure and properties of engineering alloys* (pp. 18–19). New York, NY: McGraw-Hill.

52. Grange, R. A., Lambert, V. E., and Harrington, J. J. (1959). Effective copper and heat training characteristics of medium carbon steel. *Transactions of the American Society of Metals, 51*, 377-387.

53. Grange, R. A., and Kiefer, J. M. (1941). Transformation of austenite on continuous cooling and its relation to transformation at constant temperature. *Transactions of the American Society of Metals, 29*, 85-114.

54. zur Lippe, C. F., and Grozier, J. D. (1969). In P. G. Shewmon (Ed.), *Transformations in metals* (p. 250). New York, NY: McGraw-Hill.

55. Kurita, M., and Toyama, K. (1994). Effects of strengthening mechanisms on fatigue properties of ferrite-pearlite hot-rolled sheet steel. *Tetsu-to-Hagané (Journal of the Iron and Steel Institute of Japan), 80*, 66-71.

56. Shin, J.-C., Lee, S., and Ryu, J. H. (1999). Correlation of microstructure and fatigue properties of two high-strength spring steels. *International Journal of Fatigue, 21*, 571-579.

57. Hong, Y., Qiao, Y., Liu, N., and Zheng, X. (1998). Effect of grain size on collective damage of short cracks and fatigue life estimation for a stainless steel. *Fatigue and Fracture of Engineering Materials and Structures, 21*, 1317-1325.

58. Turnbull, A., and De Los Rios, E. R. (1995). The effect of grain size, strain, and temperature on the monotonic stress-strain behaviour of polycrystalline aluminum and AL alloys. *Fatigue and Fracture of Engineering Materials and Structures, 18*,

1355-1366.

59. Yang, F., Saxena, A., and Riester, L. (1998). Use of the nanoindentation technique for studying microstructure/crack interactions in the fatigue of 4340 steel. *Metallurgical and Materials Transactions A—Physical Metallurgy and Materials Science, 29*, 3029-3036.

60. Hussain, K., and De Los Rios, R. R. (1997). Microstructural effect on tensile and fatigue behaviour of C–Mn steel. *Journal of Materials Science, 32*, 3565-3569.

61. Noniura, I. (1997). Influences of microstructures of fatigue strength of medium carbon microalloyed steels. *Tetsu-to-Hagané (Journal of the Iron and Steel Institute of Japan), 83*, 227-232.

62. Rosenberg, G. (1996). The influence of grain size, temperature, and stress state on brittle fracture of steel (in Slovak). *Metallic Materials, 34*, 201-216.

63. Sugino, K., Kageyama, H., Kuroki, T., Urashima, C., and Kikuchi, A. (1996). Metallurgical investigation of transverse defects in worn rails in service. *Wear, 191*, 141-148.

64. Ahlbeck, D. R., Harrison, H. D., Prause, R. H., and Johnson, M. R. (1976). *Evaluation of analytical and experimental methodologies for the characterization of wheel/rail loads* (U.S. Department of Transportation Report No. FRA/ORD-76/276). Springfield, VA: National Technical Information Service.

65. Broek, D., and Rice, R. C. (1977). Prediction of fatigue-crack growth in railroad rails. In Proceedings from the Ninth National Society for the Advancement of Material and Process Engineering Technology Conference [4–6 Oct. 1977, Atlanta, Georgia] (Report No. NSTC V9, Vol. 9, pp. 392–408). Covina, CA: Society for the Advancement of Material and Process Engineering.

66. Orringer, O., Morris, J. M., and Steele, R. K. (1984). Applied research on rail fatigue and fracture in the United States. *Theoretical and Applied Fracture Mechanics, 1*, 23–49.

67. Dings, P. C., and Dittrich, M. G. (1996). Roughness on Dutch railway wheels and rails. *Journal of Sound and Vibration, 193*, 103-112.

68. Orringer, O., Morris, J. M., and Jeong, D. Y. (1986). Detail fracture growth in rails: Test results. *Theoretical and Applied Fracture Mechanics, 5*, 63–95.

69. Rice, R. C. (1994). Shell and detail fracture formation in railroad rails. In R. I. Stephens (Ed.), *Case studies for fatigue education* (ASTM STP 1250) (pp. 109-138). West Conshohocken, PA: American Society for Testing and Materials.

70. Johns, T. G., and Davis, K. B. (1976). *A preliminary description of stress in railroad rails* (U.S. Department of Transportation Report No. FRA/ORD-76/294). Springfield, VA: National Technical Information Service.

71. Zhang, Z., Udpa, L., Udpa, S. S., Athavale, A. S., Utrata, D., Si, J. T., and Sun, Y. H. (1996). Linearized MFL model for embedded flaw detection in rails. In D. O. Thompson and D. E. Chimenti (Eds.), *Review of progress in quantitative nondestructive evaluation* (Vol. 15A/B) (pp. 553-560). New York, NY: Springer.

72. Orringer, O. (1988). Rail testing: Strategies for safe and economical rail quality assurance. In *Rail replacement and maintenance management* (pp. 28–42). Washington, DC: Transportation Research Board.

73. Clayton, P. (1995). Predicting the wear of rails on curves from laboratory data. *Wear*, *181*, 11-19.

74. Moyar, G. J., and Cruse, W. J. (1982). *Wear behavior of insulated joints: First FAST experiment* (U.S. Department of Transportation Report No. FRA/TTC-82/02). Springfield, VA: National Technical Information Service.

75. Wolfe, T., Spiegelberg, W., and Evangelisti, M. (1995). Exploratory metallurgical evaluation of worn rails from a 90 mm electromagnetic railgun. *IEEE Transactions on Magnetics*, *31*, Part 1, 770-775.

76. Jeong, D. Y., Tang, Y. H., and Orringer, O. (1998). *Estimation of rail wear limits based on rail strength investigations* (U.S. Department of Transportation Report No. DOT/FRA/ORD-98/07). Washington, DC: Federal Railroad Administration, Office of Research and Development. http://www.fra.dot.gov/downloads/Research/ord9807.pdf.

77. Dimelfi, R. J., Sanders, P. G., Hunter, B., Eastman, J. A., Sawley, K. J., Leong, K. H., and Kramer, J. M. (1998). Mitigation of subsurface crack propagation in railroad rails by laser surface modification. *Surface and Coatings Technology*, *106*, 30-43.

78. Bogy, D. B., Yun, X. H., and Knapp, B. J. (1994). Enhancement of head-disk interface durability by use of diamond-like carbon overcoats on the slider's rails. *IEEE Transactions on Magnetics*, *30*, 369-373.

79. Wong, S. L., Bold, P. E., Brown, M. W., and Allen, R. J. (1996). A branch criterion for shallow angled rolling contact fatigue cracks in rails. *Wear*, *191*, 45-53.

80. Duncan, A. J., Subramanian, K. H., Sindelar, R. L., Miller, K., Reynolds, A. P., and Chao, Y. J. (2002). *Development of mechanical properties database of A285 steel for structural analysis of waste tanks* (U.S. Department of Energy Report No. WSRC-MS-20000-00403 prepared under Contract No. DE-AC09-96SR18500). http://sti.srs.gov/fulltext/ms2000403/ms2000403.html.

81. Paris, P. C., and Erdogan, F. (1963). A critical analysis of crack propagation laws. *Journal of Basic Engineering*, *85*, 528–534.

82. Arad, S., Radon, J. C., and Culver, L. E. (1971). Fatigue crack propagation in polymethylmethacrylate; the effect of the mean value of stress intensity factor. *Journal of Mechanical Engineering Science*, *13*, 75–81.

83. Radon, J. C., Arad, S., and Culver, L. E. (1974). Growth of fatigue cracks in metals and polymers. *Engineering Fracture Mechanics*, *6*, 195–208.

84. Branco, C. A. M., Radon, J. C., and Culver, L. E. (1975). An analysis of the influence of mean stress intensity and environment on fatigue crack growth in a new high strength aluminum alloy. *Journal of Testing and Evaluation*, *3*, 407–413.

85. Jeong, D. Y., Tang, Y. H., Orringer, O., and Perlman, A. B. (1998). *Propagation analysis of transverse defects originating at the lower gage corner of rail* (U.S Department of Transportation Report No. DOT/FRA/ORD-98/06). Washington DC:

Federal Railroad Administration, Office of Research and Development. http://www.fra.dot.gov/downloads/Research/ord9806.pdf.

86. Walker, E. K. (1970). The effect of stress ratio during crack propagation and fatigue for 2024-T3 and 7075-T6 aluminum. In M. S. Rosenfeld (Ed.), *Effects of environment and complex load history on fatigue life* (ASTM STP 462) (pp. 1–14). West Conshohocken, PA: American Society for Testing and Materials.

87. Jeong, D. Y., Tang, Y. H., and Orringer O. (1997). Damage tolerance analysis of detail fractures in rail. *Theoretical and Applied Fracture Mechanics*, *28*, 109-115.

Abbreviations and Acronyms

½ T	compact tension specimen
a/W	notch depth to sample width ratio
AMS	austenitic manganese steel
ASTM	American Society of Testing and Materials
BCC	body-centered cubic
BLE	Brotherhood of Locomotive Engineers
EDM	electrical discharge machining
FCC	face-centered cubic
FCP	fatigue crack propagation
HB	Brinell hardness
HLC	Leeb Hardness test
HV	Vickers hardness
K_{Ic}	fracture toughness analysis
kN	kilonewton
min	minute(s)
mm	milliliter(s)
MPa √m	megapascal-sqaure root meter
s	second(s)
SEM	scanning electron microscopy
wt%	weight percent